Article

Neuron

Dynamic Palmitoylation Targets MAP6 to the Axon to Promote Microtubule Stabilization during Neuronal Polarization

Highlights

- MAP6 localizes to the Golgi complex and secretory vesicles in unpolarized neurons
- Palmitoylated MAP6 targets to the newly formed axon, where it stabilizes microtubules
- ABHD17 depalmitoylating enzymes control MAP6 membrane-microtubule shuttling
- MAP6 mediates organelle trafficking and axon maturation in vitro and in situ

Authors

Elena Tortosa, Youri Adolfs, Masaki Fukata, R. Jeroen Pasterkamp, Lukas C. Kapitein, Casper C. Hoogenraad

Correspondence

c.hoogenraad@uu.nl

In Brief

Tortosa et al. show that MAP6 re-distributes from Golgi and secretory vesicles to axonal microtubules during neuronal polarization. Palmitoylation cycles control MAP6 membrane-microtubule shuttling. The authors also demonstrate the importance of MAP6 for microtubule stabilization, organelle trafficking, and axon maturation.

Tortosa et al., 2017, Neuron *94*, 809–825
May 17, 2017
http://dx.doi.org/10.1016/j.neuron.2017.04.042

CellPress

Neuron
Article

Dynamic Palmitoylation Targets MAP6 to the Axon to Promote Microtubule Stabilization during Neuronal Polarization

Elena Tortosa,[1] Youri Adolfs,[2] Masaki Fukata,[3] R. Jeroen Pasterkamp,[2] Lukas C. Kapitein,[1] and Casper C. Hoogenraad[1,4,*]
[1]Cell Biology, Department of Biology, Faculty of Science, Utrecht University, 3584 CH Utrecht, the Netherlands
[2]Department of Translational Neuroscience, Brain Center Rudolf Magnus, University Medical Center Utrecht, 3584 CG Utrecht, the Netherlands
[3]Division of Membrane Physiology, Department of Molecular and Cellular Physiology, National Institute for Physiological Sciences, National Institutes of Natural Sciences, Okazaki, Aichi 444-8787, Japan
[4]Lead Contact
*Correspondence: c.hoogenraad@uu.nl
http://dx.doi.org/10.1016/j.neuron.2017.04.042

SUMMARY

Microtubule-associated proteins (MAPs) are main candidates to stabilize neuronal microtubules, playing an important role in establishing axon-dendrite polarity. However, how MAPs are selectively targeted to specific neuronal compartments remains poorly understood. Here, we show specific localization of microtubule-associated protein 6 (MAP6)/stable tubule-only polypeptide (STOP) throughout neuronal maturation and its role in axonal development. In unpolarized neurons, MAP6 is present at the Golgi complex and in secretory vesicles. As neurons mature, MAP6 is translocated to the proximal axon, where it binds and stabilizes microtubules. Further, we demonstrate that dynamic palmitoylation, mediated by the family of α/β Hydrolase domain-containing protein 17 (ABHD17A-C) depalmitoylating enzymes, controls shuttling of MAP6 between membranes and microtubules and is required for MAP6 retention in axons. We propose a model in which MAP6's palmitoylation mediates microtubule stabilization, allows efficient organelle trafficking, and controls axon maturation in vitro and in situ.

INTRODUCTION

The majority of neurons display a polarized morphology with two structurally and functionally well-defined compartments. Several short and branched dendrites receive information, while a thin and long axon is responsible for transmitting a message to other neurons. During early stages of neuronal development, axon formation is a crucial step in breaking symmetry and establishing neuronal polarization. Microtubules are a major determinant in the establishment of the axon and, because of their inherent polarity, are well suited to provide the structural basis for neuronal polarization (Kapitein and Hoogenraad, 2015). Several studies have identified signaling factors that regulate this process, many of which converge onto the cytoskeleton (Arimura and Kaibuchi, 2007). However, the molecular processes that control microtubule organization and remodeling during the initial stages of neuronal polarization remain elusive.

Axon initiation and outgrowth are characterized by the formation of stable and uniform parallel microtubule bundles with their plus-ends pointing outward toward the growth cone (Baas and Lin, 2011). These bundled microtubules may provide the mechanical forces that drive axon elongation in neurons (van Beuningen and Hoogenraad, 2016). Interestingly, axonal microtubules are stabilized before axon elongation and remain stable during the subsequent stages of neuronal development (Baas et al., 1991; Kollins et al., 2009; Witte et al., 2008; Yau et al., 2016). It has been shown that local stabilization of microtubules using the microtubule-stabilizing drug paclitaxel is sufficient to break symmetry and specify axon formation in unpolarized neurons (Witte et al., 2008). Moreover, paclitaxel-induced microtubule stabilization induces the formation of multiple axons out of differentiated dendrites in fully mature neurons (Gomis-Rüth et al., 2008). Thus, although it is clear that stabilizing microtubules is a key process during axon formation, little is known about the mechanisms that stabilize axonal microtubules throughout development.

An important challenge is to identify factors that control neuronal polarization by setting up axon-specific microtubule stabilization. A large variety of microtubule-associated proteins (MAPs) have been characterized and they are main candidates to mediate microtubule stabilization. MAPs are found along neuronal microtubules arrays and regulate microtubule polymerization, bundling, and/or stabilization. Interestingly, many of these proteins present specific localizations in the neuron during the different stages of neuronal development (Conde and Cáceres, 2009). Although the precise localization is likely crucial for their proper function, how MAPs are specifically localized in different compartments still remains elusive. A combination of several mechanisms, including differential protein stability and turnover, specific localization of mRNAs, or the suppression of axon-dendrite sorting have been proposed to play a role in the

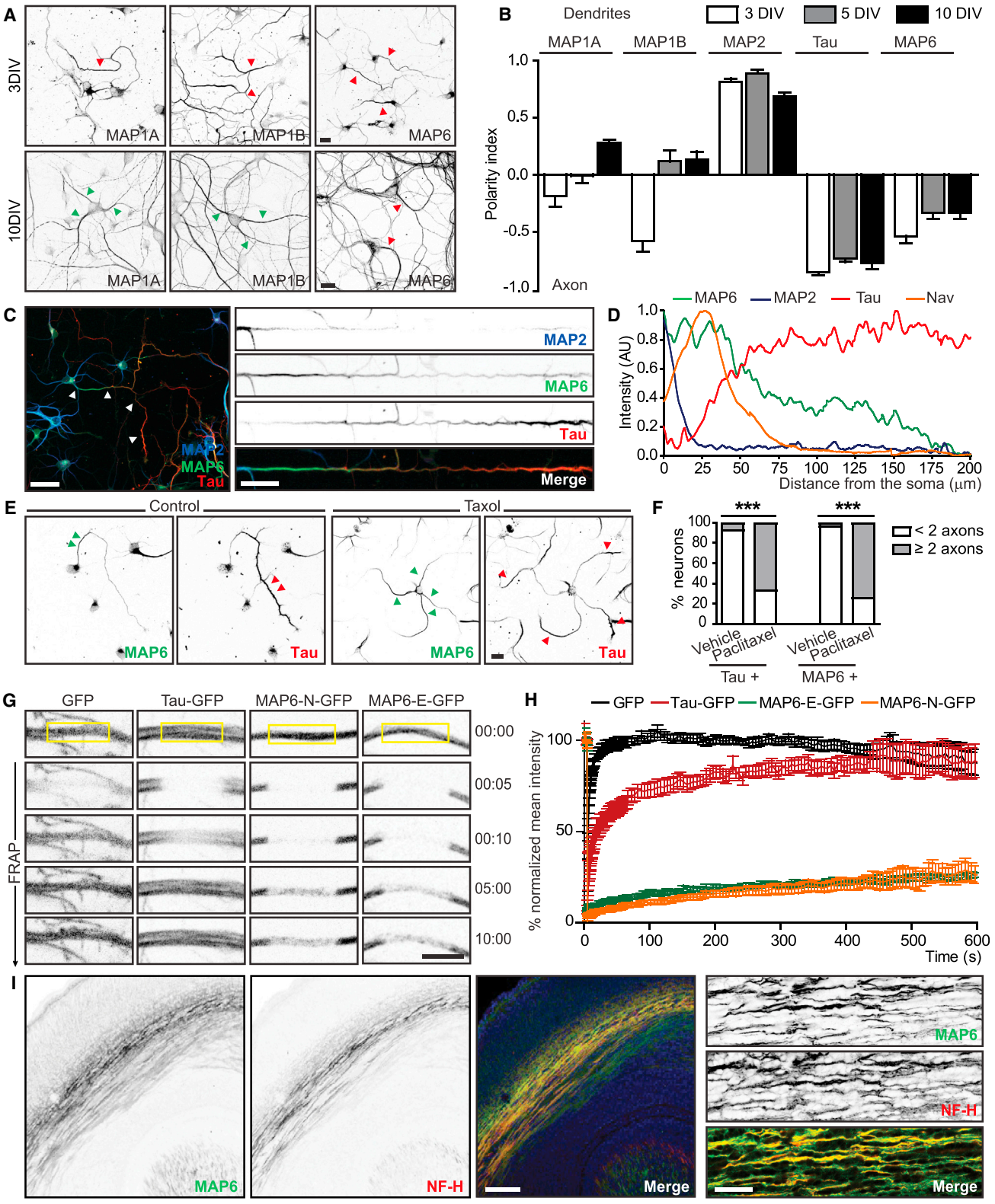

Figure 1. MAP6 Forms a Stable Compartment in the Proximal Axon

(A) Representative images of 3DIV and 10DIV neurons stained with antibodies against endogenous MAP1A, MAP1B, and MAP6.

(B) PI of the different MAPs in 3DIV, 5DIV, and 10DIV hippocampal neurons (n = 9–39 neurons).

(legend continued on next page)

polarization of MAPs, like MAP2 and Tau (Garner et al., 1988; Hirokawa et al., 1996; Kanai and Hirokawa, 1995; Li et al., 2011; Okabe and Hirokawa, 1989).

MAP6, also known as STOP (stable tubule only peptides), is particularly interesting because it is enriched in axons and has powerful microtubule stabilizing activity. In particular, MAP6 is responsible for the resistance of neuronal microtubules to cold and the microtubule-destabilizing drug nocodazole (Bosc et al., 1996; Guillaud et al., 1998). Interestingly, MAP6-depleted mice show schizophrenic-like behaviors, which can be suppressed by the microtubule-stabilizing drug epothilone D (Andrieux et al., 2002; Fournet et al., 2012). Therefore, it is of interest to understand how MAP6 is targeted to axonal microtubules and explore its potential role as microtubule stabilizer in neuronal development.

In this study, we demonstrate that MAP6 is present at the Golgi complex and in secretory vesicles in unpolarized cells and redistributed to newly forming axons, where it binds and stabilizes axonal microtubules. A palmitoylation cycle controls MAP6 membrane-microtubule shuttling and is required for its polarized distribution in axons. Our results reveal a regulatory role for MAP6 in stabilizing axonal microtubules and coordinating KIF5-mediated axonal transport during neuronal development and provide evidences for a new mechanism of axonal targeting.

RESULTS

MAP6 Forms a Stable Compartment in the Proximal Axon

In order to identify MAPs responsible for stabilizing axonal microtubules during neuronal development, we first analyzed the polarized distribution of several MAPs in hippocampal neurons by measuring the dendrite-to-axon ratio and calculated the polarity index (PI) (Kapitein et al., 2010). Interestingly, MAPs like MAP1A and MAP1B switched from axonal to a more dendritic polarized distribution during neuronal maturation. Others like MAP6 and Tau were highly enriched in the axonal compartment. In agreement with published data (Schwenk et al., 2014), some dendritic staining for MAP6 was observed, becoming more prominent in more mature neurons (Figures 1A, 1B, S1A, and S1B). Interestingly, MAP6 showed a preferential localization in the more proximal part of the axon, while Tau was enriched at the distal region (Figures 1C, 1D, and S1C). Consistently, MAP6 and Tau proteins relocated to newly formed axons after paclitaxel treatments and separated into distinct axonal domains (Figures 1E and 1F). To determine the dynamics of both proteins in axons, we performed fluorescence recovery after photobleaching (FRAP) analysis of GFP-tagged Tau and both neuronal MAP6 isoforms, MAP6-E and MAP6-N. The fluorescence recovery of both MAP6 isoforms was remarkably slow and incomplete when compared to Tau (Figures 1G and 1H), indicating that a large fraction of MAP6 molecules is highly immobile and that MAP6 forms a relatively stable compartment in the proximal axon. In agreement with these data, immunofluorescence of embryonic brain sections showed that MAP6 was highly enriched in axons from the hippocampus and corpus callosum, overlapping with the axonal marker high molecular weight neurofilament subunit (NF-H) (Figure 1I). MAP6 features interesting microtubule stabilizing properties and, while Tau has been studied extensively before (Dawson et al., 2001; Takei et al., 2000), MAP6 function in neurons is not well understood (Bosc et al., 1996; Guillaud et al., 1998). Therefore, we focused on MAP6 and its role as axonal microtubule stabilizer during neuronal polarization.

MAP6 Stabilizes Microtubules in the Axonal Compartment

Previous works show that MAP6 localizes along neuronal microtubule arrays in axons (Guillaud et al., 1998; Slaughter and Black, 2003). We further examined the interaction between MAP6 and microtubules, and its relevance for axonal microtubule organization. MAP6-GFP expression in COS-7 cells labeled a subset of stable (detyrosinated and acetylated) microtubules (Figures 2A–2C). Similar results were obtained in neurons where both endogenous MAP6 and overexpressed MAP6-GFP coincided with stable microtubule bundles (Figure 2D). Neurons transfected with MAP6 shRNAs and stained for EB1 as a marker for dynamic microtubules showed an increased number of the characteristic comets marking microtubules plus-end in soma, whereas no differences were detected in dendrites (Figures 2E, 2F, S2A, and S2B). Further, when we visualized microtubule growth by using the plus-end marker GFP-MT+TIP in axons, we observed a similar increase in dynamic microtubules upon MAP6 depletion in axons (Figure 2G). We did not detect any differences in microtubule orientation, growth rate, time, or run length between MAP6 knockdown and control neurons (Figures S2C and S2D). Consistently, the staining for detyrosinated tubulin was reduced, whereas levels of tyrosinated tubulin were unaltered in neurons depleted of MAP6 (Figures 2H, 2I, and S2E). Additionally, FRAP experiments examining the recovery of β-tubulin-GFP confirmed that axonal microtubules were less stable in MAP6-depleted neurons (Figures 2J and 2K). Overall, our data suggest that MAP6 stabilizes axonal microtubules.

MAP6 Promotes KIF5-Mediated Organelle Trafficking in Axons

Previous studies showed that kinesin-1/KIF5-mediated transport has high affinity for stabilized and/or modified microtubules

(C) Representative images and straightened zooms of 4DIV hippocampal neurons co-stained for MAP2, MAP6, and Tau.
(D) Diagram showing the average normalized fluorescent intensity profiles of MAP6, MAP2, Tau, and Na_v channels (n = 12–25 neurons).
(E) Representative images of 3DIV hippocampal neurons treated with control vehicle (DMSO) or 10 nM paclitaxel for 24 hr and co-stained for MAP6 and Tau.
(F) Percentage of neurons with <2 or ≥2 neurites positive for Tau or MAP6 (n = 48–81 neurons; Fisher's exact test).
(G) FRAP of GFP, GFP-Tau, or MAP6-E-GFP and MAP6-N-GFP expressed in DIV5 hippocampal neurons. Time is shown in minutes.
(H) Average normalized intensity graph of FRAP of indicated constructs in DIV5 hippocampal neurons (n = 10–14 neurons).
(I) Brain sections stained for MAP6 together with neurofilament heavy chain (NF-H) and DAPI. Right panels show higher magnifications.
Red and green arrowheads point to axons and dendrites, respectively. Graphs represent mean ± SEM in (B) and (H). Scale bar represents 100 μm in (I), 40 μm in zooms in (I), 20 μm in (A), (C), and (E), 10 μm in zooms in (C), and 5 μm in (G). See also Figure S1.

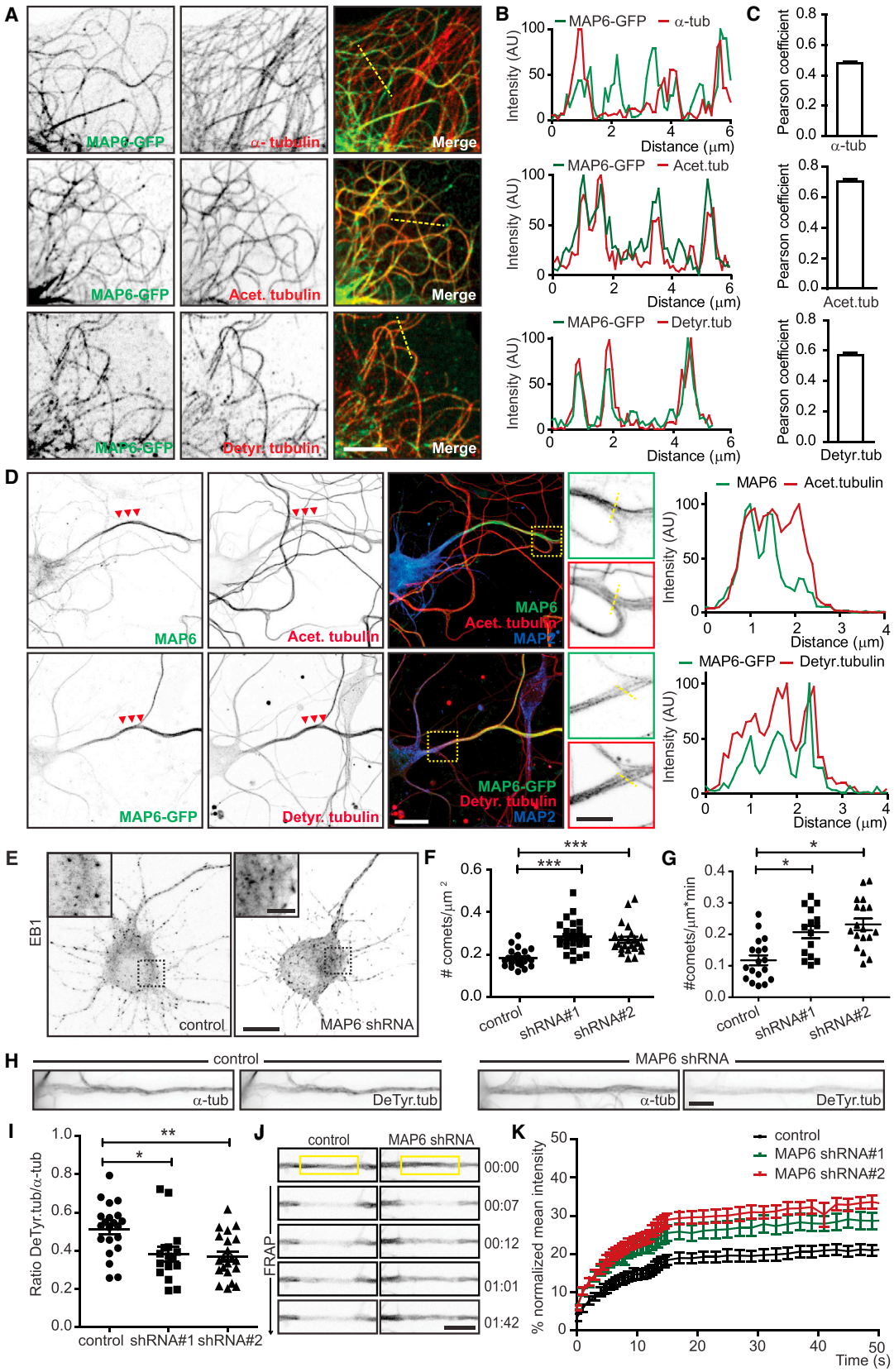

(legend on next page)

(Cai et al., 2009; Nakata and Hirokawa, 2003). Hence, we tested how MAP6-stabilized microtubules influence KIF5-based mitochondrial trafficking by using live-cell imaging of Mito-dsRed. In the absence of MAP6, mitochondrial motility in axons was reduced by ~25% (Figures 3A). While the velocity did not change, the duration and length of the mitochondrial runs decreased (Figure S3A). MAP6 depletion affected both the anterograde and retrograde transport parameters (Figure S3B), suggesting that MAP6 plays a role in coordinating bidirectional axonal transport. Interestingly, co-expression of KIF5B-GFP together with MAP6-mCherry in MRC-5 cell line suggests that KIF5B preferentially moves on MAP6-positive microtubules (Figures S3C–S3E). Additionally, the number of runs for KIF5B-GFP slightly increased in MAP6-labeled microtubules when compared to control (Figures S3F and S3G). Consistently, MAP6 knockdown decreased the number of runs for KIF5B-GFP in neurons (Figure 3B). We did not detect any differences in KIF5B-GFP velocities in both MAP6 knockdown and overexpression (Figures S3H and S3I). Finally, using the inducible cargo trafficking assay, we also found strongly reduced KIF5-driven cargo runs in axons of MAP6 knockdown neurons (Figure S3J). Together, the data suggest that MAP6 promotes KIF5-mediated axonal cargo transport.

MAP6 Controls Axon Maturation In Vitro and In Situ

To further study the function of MAP6 in neurons, we next determined whether MAP6 plays a role in axon growth. We performed shRNA knockdowns of several MAPs in polarized hippocampal neurons and used paclitaxel to induce the formation of new axons (Gomis-Rüth et al., 2008; Witte et al., 2008). Most cultured hippocampal neurons at 6 days in vitro (DIV6) presented one axon, which was identified by the presence of voltage-gated sodium channels (Na_v), an axon initial segment (AIS) marker. Treatments with low concentrations of paclitaxel strongly increased the number of neurons with multiple axons. In contrast to MAP2-depleted cells, paclitaxel-induced axonal processes did not emerge in neurons lacking Tau or MAP6, suggesting a role for these two MAPs in axon formation (Figures S4A–S4C). To further determine whether MAP6 is involved in axon growth during the initial stages of neuronal polarization, we electroporated cortical neurons with several MAP6 shRNAs and stained for various axonal makers at DIV3–DIV4. While most MAP6 knockdown neurons were positive for the early axonal markers Tau and TRIM46 (Figures 3C and 3E), the AIS (as visualized by Na_v channels) was largely absent (Figures 3D and 3F). The AIS phenotype was rescued by overexpressing MAP6-GFP in MAP6-depleted neurons (Figure 3F). Consistent with an axonal defect, we observed a marked reduction in the total axonal length in MAP6 knockdown neurons (Figure 3G).

Finally, we examined whether MAP6 plays a role during neuron polarization in situ. Mouse brains were electroporated in utero at E14.5 with control and MAP6 shRNAs, together with GFP to visualize neuronal morphology. Control neurons efficiently migrated to the upper layers of the cortical plate and developed a typical bipolar morphology with a leading process and a trailing edge. In contrast, MAP6-depleted neurons failed to migrate properly and accumulated in the ventricular and subventricular zones (Figures 3H and 3I). Interestingly, upon MAP6 depletion most of the neurons seemed to be properly orientated. However, fewer neurons displayed the typical bipolar morphology; many neurons seemed to display shorter leading processes and often lacked the trailing processes (Figures 3J and 3K). Altogether, these data demonstrate the role of MAP6 in axon maturation and neuronal migration. However, since both neuronal migration and axon maturation are strongly dependent on each other, we cannot rule out that the observed axonal phenotype in situ is caused by abnormal cell migration.

MAP6 Is Present at the Golgi Apparatus and Secretory Vesicles

In addition to its axonal localization, MAP6 has also been reported to associate with the Golgi apparatus and vesicular structures (Gory-Fauré et al., 2006, 2014). Indeed, at DIV4, we detected MAP6 in axons, at the Golgi complex in the cell body, as well as in vesicles that accumulate at the tip of some neurites (Figure 4A). We observed similar results upon expression of MAP6-GFP in cultured neurons (Figure 4B). Subsequently, we investigated the identity of the MAP6-positive vesicles by staining for various vesicular markers, including secretory vesicles (Rab6), lysosomes (LAMP1), and synaptic precursor vesicles (Rab3). In unpolarized neurons, MAP6 strongly co-localized with Rab6-positive secretory vesicles and was excluded from

Figure 2. MAP6 Stabilizes Microtubules in the Axonal Compartment

(A) COS-7 cells expressing MAP6-GFP and stained for α-, acetylated, and detyrosinated tubulin.

(B) Line scans for MAP6-GFP and tubulins from previous examples.

(C) Colocalization analysis using Pearson's correlation coefficient.

(D) Representative images and zooms of neurons co-stained for enogenous MAP6 together with acetylated tubulin and MAP2, or expressing MAP6-GFP and co-stained for GFP, detyrosinated tubulin, and MAP2. Arrowheads point to axons. On the right, line scans for MAP6 and tubulins from previous examples are shown.

(E) Representative images and zooms of DIV4 hippocampal neurons transfected with a plasmid control or MAP6-shRNA#1 and stained for EB1.

(F and G) Average dynamic microtubule (comets) density in soma of fixed hippocampal neurons (n = 23–25 neurons; Kruskal-Wallis test followed by a Dunn's Multiple Comparison Test) (F) and the proximal axon of living hippocampal neurons (n = 15–18 neurons; one-way ANOVA followed by a Tukey's multiple comparison test) (G) transfected with a plasmid control or MAP6-shRNAs and cultured for 4DIV.

(H) Representative images of DIV4 neurons nucleofected with a plasmid control or MAP6-shRNA#1, and stained for α- and detyrosinated tubulin.

(I) Detyrosinated tubulin mean intensity in axons of neurons expressing a plasmid control or MAP6-shRNAs (n = 23–25 neurons; Kruskal-Wallis test followed by a Dunn's Multiple Comparison Test).

(J) FRAP of β-tubulin expressed in 4DIV hippocampal neurons, together with a plasmid control or MAP6-shRNAs. Time in minutes.

(K) Average normalized intensity graph of FRAP of tubulin in plasmid control, MAP6-shRNA#1, or MAP6-shRNA#2 transfected neurons (n = 11–16 neurons). Graphs represent mean ± SEM in (C), (F), (G), (I), and (K). Scale bar represents 20 μm in (D), 10 μm in (E), 5 μm in (A), (H), (J), and zooms in (D), and 3 μm in zooms in (E). See also Figure S2.

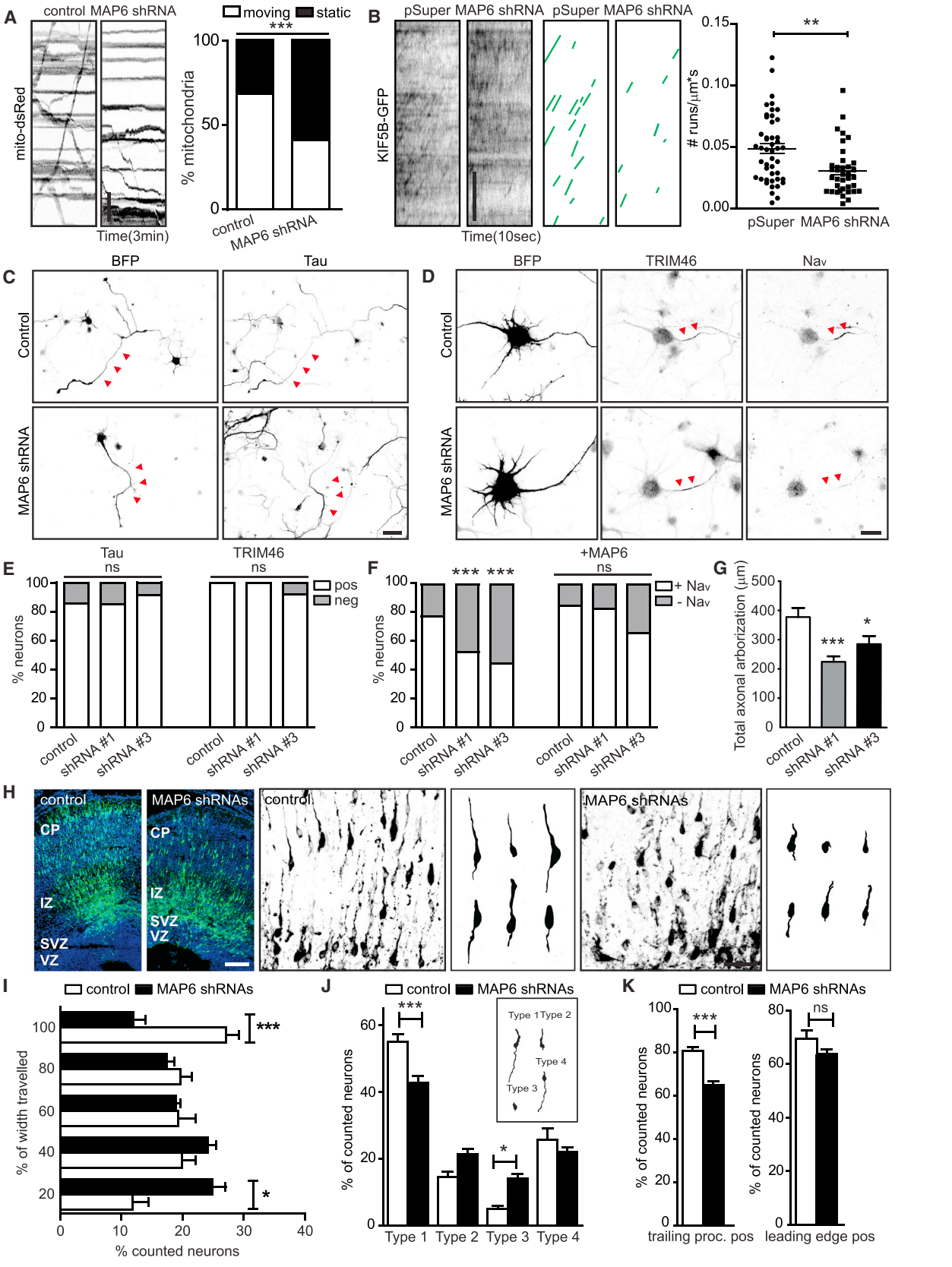

(legend on next page)

the lysosome and synaptic vesicle populations (Figures 4C, 4E, S5A, and S5B). MAP6-labeled vesicles were also positive for other secretory markers, such as neuropeptide Y (NPY), and coincided with the palmitoylated stathmin-related proteins SCG10 and proto-oncogene N-Ras (Figures 4C, 4E, S5C, and S5D). Co-localization between MAP6 and Rab6 or SCG10-positive vesicles was maintained after axon formation (Figures S5E and S5F). In agreement with these findings, live cell imaging of MAP6-GFP and RFP-Rab6 or NPY-RFP showed the same co-localization pattern (Figures 4D, 4F–4H, and S5G–S5I; Movie S1). These data show that MAP6 is present in the axon and at the Golgi complex and secretory vesicles in developing neurons.

MAP6 Becomes Highly Enriched in Axons during Neuronal Polarization

Given the differential MAP6 localizations in unpolarized and polarized neurons, we decided to analyze in more detail the expression and distribution of MAP6 during early stages of neuronal development. Western blot analysis of embryonic and postnatal brains and hippocampal neuron culture extracts showed that the MAP6 isoform MAP6-E was expressed in the brain at early embryonic stages and, in dissociated neurons, before neuronal polarization (DIV1), with increased expression as the development progressed. The other neuronal MAP6 isoform, MAP6-N, was expressed only after birth and in more mature neurons in culture (Figures 5A and 5B). By co-staining unpolarized (stage 2) and polarized (stage 3) neurons with markers for the axon (Tau), AIS (Na_v channels), and Golgi apparatus (GM130), we studied MAP6 distribution during neuronal polarization. In unpolarized cells, MAP6 was present at the Golgi complex (Figures 5C and 5D). Directly following the polarization, MAP6 became enriched in Tau-positive and AIS-negative axons (Figures 5E, 5F, and S5J). These results show that MAP6 is enriched in developing axons before AIS formation. Consistently with previous observations (Schwenk et al., 2014), MAP6 was more prominently present in dendrites in more mature neurons (stage 4), although it remained enriched in axons (Figures 5G and 5H). We corroborated those results by imaging MAP6-GFP vesicle dynamics during development. In unpolarized cells, MAP6 vesicles accumulated transiently at the tips of a subset of neurites and dynamically translocated between them (Figures 5I, 5J, and 5L; Movie S2). During axon outgrowth, MAP6 vesicles first accumulated in the axonal growth cone while, over time, MAP6 became highly enriched throughout the axon (Figures 5I, 5K, 5M, 5N, and S5K; Movie S2). Our results show that MAP6 is targeted into the axon during neuronal polarization and raises an interesting question about the precise mechanism responsible for MAP6's redistribution.

N-Terminal Domain Palmitoylation Controls MAP6 Distribution in Neurons

Protein palmitoylation is a reversible lipid modification that facilitates protein insertion into intracellular and plasma membranes and allows proteins to rapidly shuttle between intracellular compartments (Fukata and Fukata, 2010). Previous studies have shown that palmitoylation mediates the binding of MAP6 to Golgi membranes (Gory-Fauré et al., 2006, 2014). To determine whether palmitoylation also controls the vesicular localization of MAP6 in neurons, we mutated three cysteines (Cys 5, 10, and 11) in the N-terminal region of MAP6 (MAP6-GGG) (Gory-Fauré et al., 2014). As expected, MAP6-GGG was still able to bind microtubules but did not localize either to Golgi apparatus or to secretory vesicles (Figures 6A and 6B). Interestingly, the palmitoylation-defective MAP6 mutant mislocalized to dendrites and lost the axonal enrichment observed in control (Figures 6D–6F). To further investigate whether palmitoylation is

Figure 3. MAP6 Promotes Efficient Organelle Trafficking and Controls Axon Maturation In Vitro and In Situ

(A) Representative kymographs from mito-dsRed time-lapse recordings in the axon of hippocampal neurons (DIV4) transfected with mito-dsRed and a plasmid control or MAP6-shRNA#1. On the right, percentage of moving and static particles in plasmid control or MAP6-shRNA#1-transfected neurons (n = 280–1,172 mitochondria from 28–41 neurons; Fisher's exact test).

(B) Representative kymographs and quantifications from KIF5B-GFP time-lapse recording in axons of hippocampal neurons (DIV4) co-transfected with KIF5B-GFP and a plasmid control or MAP6-shRNA#1 (n = 37–46 neurons; unpaired t test).

(C) Representative images of DIV3 cortical neurons electroporated with a plasmid control or MAP6 shRNA#1, together with BFP, and stained for Tau.

(D) Representative images of DIV4 electroporated cortical neurons with a plasmid control or MAP6 shRNA#1, together with BFP, and co-stained for TRIM46 and Na_v channels. Arrowheads point to axons in (C) and (D).

(E) Percentage of DIV3 (stained for Tau) and DIV4 (stained for TRIM46) neurons electroporated with a plasmid control or MAP6-shRNAs with neurites positive/negative for Tau (n = 21–27 neurons) and TRIM46 (n = 19–26 neurons).

(F) Percentage of neurons with neurites positive/negative for Na_v channels, electroporated with a plasmid control or MAP6-shRNAs, only with BFP (n = 93–174 neurons; Fisher's exact test with Bonferroni correction) or together with MAP6-GFP (n = 40–52 neurons; Fisher's exact test with Bonferroni correction), and cultured for 4DIV.

(G) Total axonal length of DIV3 neurons nucleofected with a plasmid control or MAP6 shRNAs (n = 20–29 neurons; one-way ANOVA followed by a Tukey's multiple comparison test).

(H) Low- and higher-magnification stitched maximum intensity projection (GFP and DAPI) and quantification of migrating neurons in E17.5 mouse cortex that were positively in utero electroporated (at E14.5) with GFP and a plasmid control or MAP6-shRNAs. CP, cortical plate; IZ, intermediate zone; SVZ, subventricular zone; VZ, ventricular zone. Right panels show individual traces of representative GFP-positive neurons.

(I) Normalized migration distribution along the radial axis of the cortex from the ventricle to the pial surface of GFP-positive neurons (n = 10–16 slices from 3 different embryos; Kruskal-Wallis test followed by a Dunn's Multiple Comparison test).

(J) Distribution of four different GFP-positive neuronal cell morphologies (n = 466–747 neurons from 3 different embryos; one-way ANOVA followed by a Tukey's multiple comparison test).

(K) Percentage of trailing process-positive (left) or leading process-positive (right) GFP-positive neurons (n = 466–747 neurons; unpaired t test).

Graphs represent mean ± SEM in (B), (G), (I), (J), and (K). Scale bar represents 200 μm in (H), 40 μm in (C), and zooms in (H), 20 μm in (D), 10 μm in (A), and 5 μm in (B). See also Figures S3 and S4.

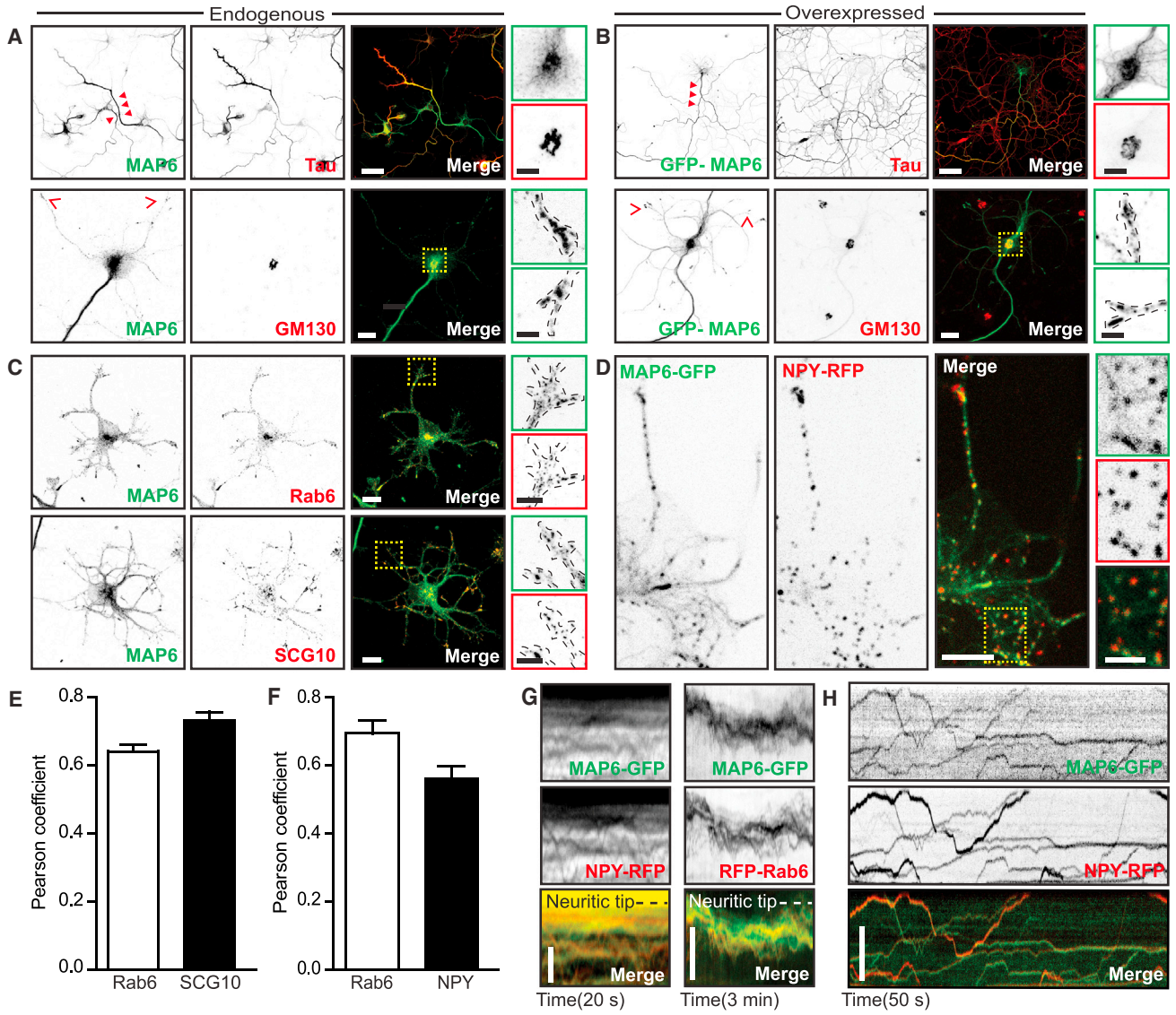

Figure 4. MAP6 Is Present in Golgi Apparatus and Secretory Vesicles

(A and B) Representative images of hippocampal neurons (DIV4) stained for endogenous MAP6 and co-stained for Tau and GM130 to highlight axons and Golgi apparatus (A) and hippocampal neurons (DIV4+1) transfected with MAP6-GFP and stained for Tau and GM130 (B). Right panels show higher magnifications of Golgi and vesicle localization of endogenous and overexpressed MAP6. Filled arrowheads point to axons and empty arrowheads point to MAP6-positive vesicles.

(C) Representative images and zooms of unpolarized hippocampal neurons co-stained for MAP6 and Rab6 (top panels) or SCG10 (bottom panels).

(D) Representative stills and zooms from MAP6-GFP and NPY-RFP time-lapse recordings of hippocampal neurons (DIV2).

(E and F) Quantification of vesicle colocalization in unpolarized neurons co-stained for MAP6 and Rab6 or SCG10 (n = 13 neurons) (E) and DIV2 neurons co-transfected with MAP6-GFP and RFP-Rab6 or NPY-RFP (n = 13 neurons) (F).

(G and H) Representative kymographs from MAP6-GFP and NPY-RFP or RFP-Rab6 time-lapse recordings in hippocampal neurons (DIV2).

Graphs represent mean ± SEM in (E) and (F). Scale bar represents 20 μm in (A, top) and (B, top), 10 μm in (A, bottom), (B, bottom), and (C), 5 μm in (D), (G, right), (H), and zooms in (A), (B), and (C), and 2 μm in (G, left) and zooms in (D). See also Figure S5.

required for MAP6 polarization, we generated GFP-tagged N-terminal, microtubule-binding, and C-terminal domains of MAP6 (Figures 6A and S5L). In contrast to the other constructs, the N-terminal domain localized to Golgi membranes and was enriched in the axon. Furthermore, when palmitoylation sites were mutated (Nterm-GGG), the N-terminal domain localized to dendrites and lost its axonal polarization (Figures 6C–6F). Despite the axonal enrichment of the N-terminal domain, the number of NPY-GFP-labeled secretory vesicles did not increase in the axon and revealed a nonpolarized distribution in DIV4 neurons (Figures 6G and 6H). This suggests that axonal MAP6 targeting is not due to a selective distribution of secretory vesicles in developing neurons. At the same time, neither MAP6 knockdown nor overexpression affected the secretory vesicle

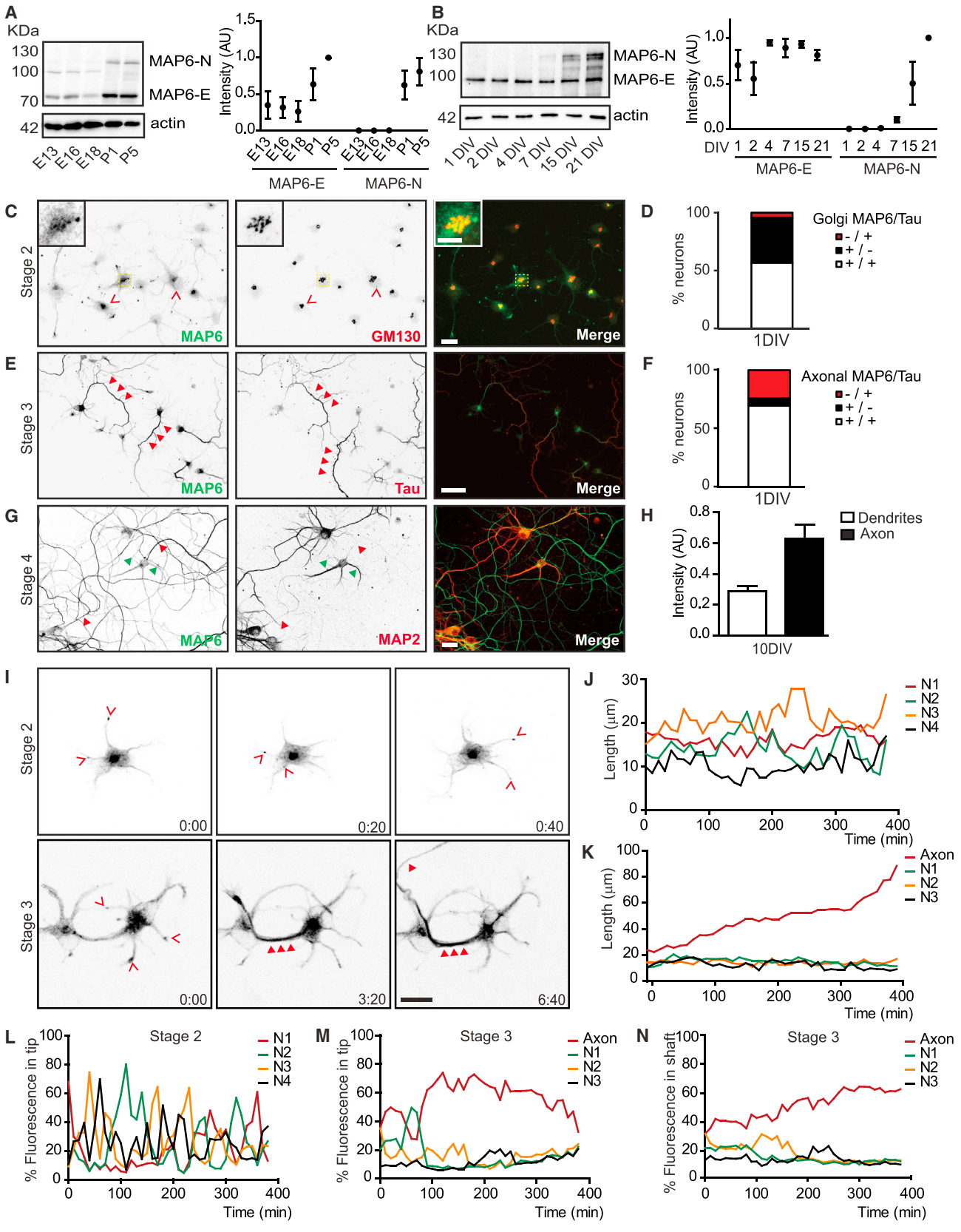

(legend on next page)

distribution (Figure 6H). Interestingly, while the N-terminal domain revealed a vesicular localization in the soma and proximal region of the axon, it had a diffuse, cytosolic distribution in the more distal regions of the axon. Conversely, NPY-positive vesicles were observed along the length of the axon, including distal regions (Figure 6I). These results indicate that palmitoylation at the N-terminal region is required to bind MAP6 to secretory vesicles and to target MAP6 to axons. Once MAP6 reaches the axon, it de-attaches from the vesicles and becomes enriched in the axon. Based on these results, we proposed that palmitoylation cycles control MAP6 localization and, consequently, its axonal polarization.

Palmitoylation Cycles Regulate MAP6 Localization and Polarization

Dynamic palmitoylation is controlled by the DHHC family of palmitoyl transferases and depalmitoylating enzymes (Fukata and Fukata, 2010). COS-7 cells transfected with MAP6-GFP and treated with Palmostatin B (PalB), an inhibitor of depalmitoylating enzymes, showed no changes in the number of MAP6-positive vesicles. However, a marked decrease in the number of microtubules labeled with MAP6-GFP was observed (Figures 7A and 7B). Likewise, treatments with 2-Bromopalmitate (2-BP), a general protein palmitoylation inhibitor, reduced the number of vesicles positive for MAP6 and strongly increased the microtubule localization as shown both in fixed and live cells (Figures 7A–7E; Movie S3). The number of Rab6-labeled secretory vesicles was not affected (Figure 7F), suggesting that MAP6 membrane-microtubule shuttling is regulated by protein palmitoylation.

We next determined whether 2-BP and PalB treatments also affect MAP6 polarized sorting in cultured neurons. Inhibition of both palmitoylation and depalmitoylation strongly reduced selective MAP6 enrichment in axons, causing a reduction in the PI by ~60% for PalB and ~35% for 2-BP (Figures 7G and 7H). To better understand how these drug treatments affect MAP6 localization to vesicles, we transfected neurons with the N-terminal domain of MAP6 fused to GFP and treated them with PalB and 2-BP. Treatments with PalB increased the number of MAP6-positive vesicles in the distal part of the axon, whereas 2-BP caused loss of N-terminal domain's vesicular localization (Figures 7I–7K). The number of NPY-positive secretory vesicles was unchanged (Figure S5M). Interestingly, disrupting intracellular calcium concentration with BAPTA or ionomycin also affected the localization of MAP6 to vesicles. BAPTA mimicked PalB treatment (Figures 7I–7K and S5M), suggesting that palmitoylation cycles may be regulated by axonal calcium flux. Together, these results demonstrate that palmitoylation cycles control not only MAP6 shuttling between secretory vesicles and microtubules, but also its axonal polarization.

ABHD17B Depalmitoylating Enzyme Controls MAP6 Palmitoylation and Mediates in Its Localization and Polarization

Depalmitoylating enzymes catalyze palmitate removal from cysteine residues, regulating protein localization and function (el-Husseini and Bredt, 2002; Fukata and Fukata, 2010). Recently, a family of depalmitoylating enzymes, α/β-Hydrolase domain-containing protein 17 members (ABHD17A, 17B, and 17C), has been found to regulate PSD95 depalmitoylation (Yokoi et al., 2016). We next tested which depalmitoylating enzymes show specificity for MAP6. COS-7 cells co-transfected with MAP6-GFP and depalmitoylating enzymes ABHD12 and 13, APT-1, and APT-2 showed no changes in the number of MAP6-positive vesicles and MAP6-labeled microtubules. However, coexpression of ABHD17 family members markedly reduced the number of vesicles positive for MAP6 and strongly increased the microtubule localization (Figure 8A). To determine whether these depalmitoylating enzymes also affect MAP6 localization in neurons, we co-expressed them together with the N-terminal domain of MAP6 fused to GFP. In agreement with COS-7 data, expression of depalmitoylating enzymes ABHD17A, B, or C all reduced the number of MAP6-positive vesicles (Figure 8B). Interestingly, overexpression of ABHD17B also affected N-terminal domain polarization in neurons (Figure 8C). The catalytically inactive mutant ABHD17B D235A has been suggested to act as a substrate-trapping mutant, inhibiting the action of endogenous depalmitoylating enzymes (Yokoi et al., 2016). Although we did not observe changes in the PI, overexpression of the mutant form markedly increased the number of MAP6-positive vesicles in the distal part of the axon (Figures 8D and S5N). Importantly, all changes observed in MAP6 localization and polarization correlated with changes in its palmitoylation levels, detected by Acyl-RAC

Figure 5. MAP6 Becomes Enriched in Axons during Neuronal Polarization

(A) Western blot analysis and relative quantification of MAP6 in protein extracts obtained from E13, E16, E18, P1, and P5 mice (n = 3 experiments).

(B) Western blot analysis and relative quantification of MAP6 levels in protein extracts obtained from DIV1, DIV2, DIV4, DIV7, DIV14, and DIV21 hippocampal neurons (n = 3 experiments). Levels of actin were used as a loading control.

(C) Representative images of DIV1 cultured hippocampal neurons stained for MAP6 and GM130. Empty arrowheads point to MAP6-positive Golgi structures.

(D) Percentage of neurons at DIV1 with Golgi MAP6 staining and one neurite positive/negative for Tau (n = 66–75 neurons).

(E) Representative images of DIV1 cultured hippocampal neurons stained for MAP6 and Tau. Filled arrowheads point to axons.

(F) Percentage of neurons at DIV1 with axonal MAP6 staining and one neurite positive/negative for Tau (n = 66–75 neurons).

(G) Representative images of DIV10 cultured hippocampal neurons stained for MAP6 and MAP2. Red arrowheads point to axons and green arrowheads dendrites.

(H) Normalized mean fluorescent intensity for MAP6 in dendrites and axons (n = 15 neurons).

(I) Representative stills from MAP6-GFP time-lapse recordings of unpolarized and polarizing hippocampal neurons (DIV1). Filled arrowheads point to axons and empty arrowheads point to MAP6-positive vesicles.

(J and K) Neurite length in an unpolarized (J) and a polarizing (K) neuron expressing MAP6-GFP (DIV1).

(L and M) Percentage of total fluorescence present at the tip of neurites in an unpolarized (L) and a polarizing (M) neuron expressing MAP6-GFP.

(N) Percentage of total fluorescence present at the shaft of neurites in a polarizing neuron expressing MAP6-GFP.

Graphs represent mean ± SEM in (A), (B), and (H). Scale bar represents 40 μm in (C) and (E), 20 μm in (G), 10 μm in (I), and 2 μm in zooms in (C). See also Figure S5.

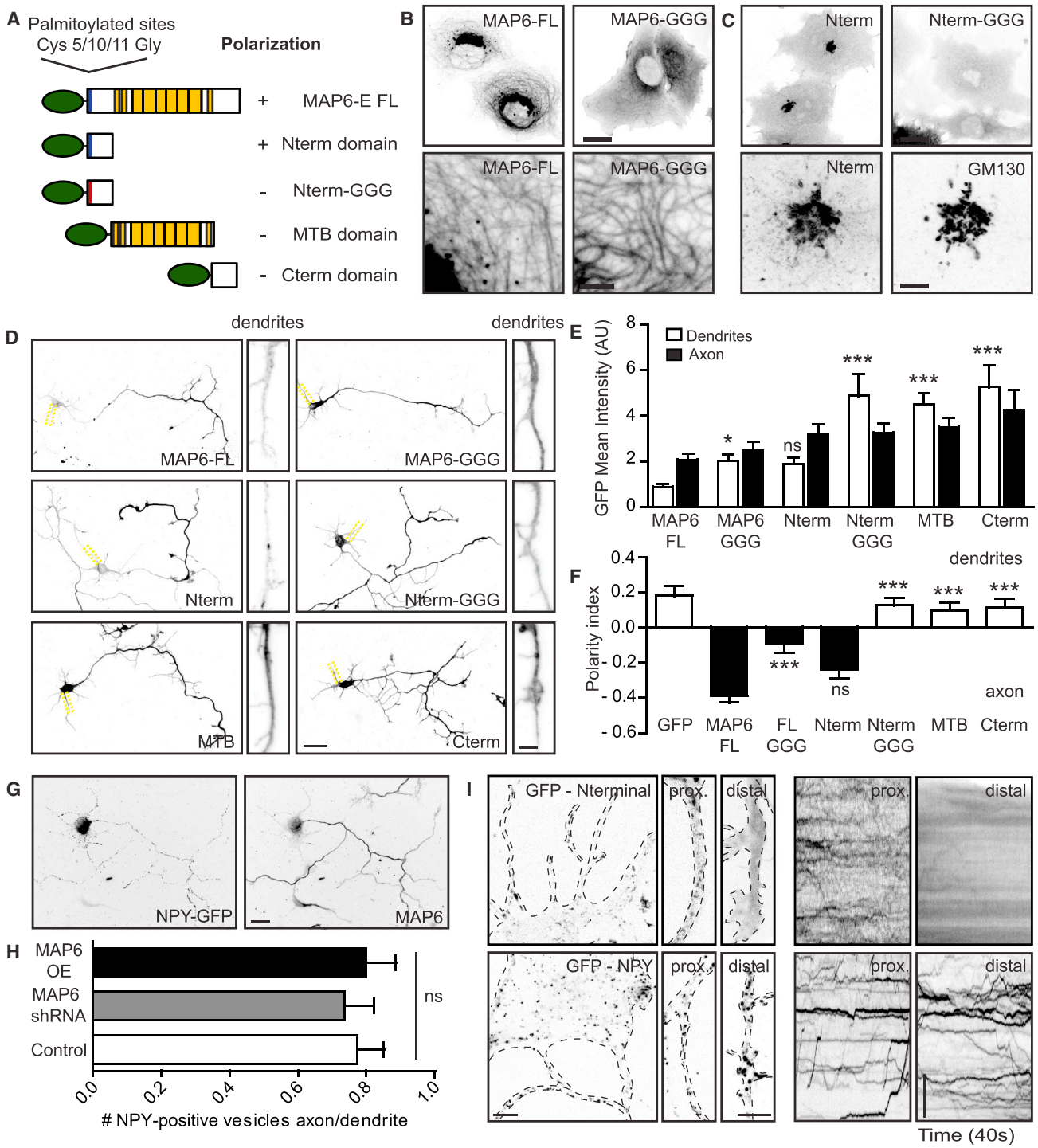

Figure 6. N-Terminal Domain Palmitoylation Controls MAP6 Distribution in Neurons

(A) Schematic diagram of MAP6 indicating palmitoylated sites and the different GFP-tagged MAP6 domains cloned. On the right, + or − indicate whether these constructs are or not enriched in axons.

(B) Representative images and zooms of COS-7 cells expressing GFP-tagged MAP6 wild-type (MAP6-FL) and MAP6 with mutated palmitoylated sites (MAP6-GGG).

(C) Representative images of COS-7 cells expressing the N-terminal domain of MAP6 (Nterm) and the N-terminal with mutated palmitoylated sites (Nterm-GGG). Bottom panels show higher magnifications of N-terminal localization in Golgi areas (stained with GM130 antibody).

(D) Representative images of neurons expressing GFP-tagged MAP6-FL, MAP6-GGG, and MAP6 domains and zoom of dendrites.

(legend continued on next page)

assays. In particular, overexpression of ABHD17B decreased the palmitoylation levels of endogenous MAP6 in neurons (Figures 8E and 8F). Finally, ABHD17B also affected endogenous MAP6 polarization in cultured neurons; ABHD17B strongly increased MAP6 enrichment in dendrites, causing a reduction in its PI (Figures 7G and 7H). In conclusion, our data strongly indicate that MAP6 depalmitoylation, mediated by the ABHD17 family members, regulates the localization of MAP6 between secretory vesicles and microtubules and controls its polarized distribution in axons.

DISCUSSION

Neuronal polarization is a highly coordinated and rigorously regulated process that requires a compartment-specific distribution of axonal and dendritic components and a complete reorganization of the microtubule cytoskeleton. Among other events, stabilization of axonal microtubules is an important step in this process. In this study, we describe the palmitoylation/depalmitoylation cycle as an important molecular process to selectively target MAP6 into axons. We demonstrate that palmitoylated MAP6 localizes to Golgi and secretory vesicles in unpolarized cells. During axon formation, MAP6 is depalmitoylated and detached from vesicles, becoming enriched in the newly formed axon. Our data suggest that the presence of MAP6 defines a specific axonal compartment, where it binds and stabilizes microtubules, regulates efficient organelle trafficking, and controls axon maturation in vitro and in situ.

Microtubule Stabilization and Axon Formation

Microtubules have emerged as crucial players in neuronal development and function (Conde and Cáceres, 2009; Hoogenraad and Bradke, 2009). MAPs have been shown to be important in neuronal polarization and are the main candidates to mediate microtubule stabilization (Poulain and Sobel, 2010). Particularly, it has been reported that MAP6/STOP is responsible for microtubule stabilization under various conditions such as exposure to cold or depolymerizing drugs (Andrieux et al., 2002; Bosc et al., 1996; Guillaud et al., 1998). Note worthily, MAP6-depleted mice are viable but they show axonal defects and display various behavioral phenotypes (Andrieux et al., 2002; Deloulme et al., 2015; Fournet et al., 2012). Interestingly, treatments with microtubule-stabilizing drugs diminished these deficits (Daoust et al., 2014; Fournet et al., 2012), indicating that MAP6 is a major candidate for mediating microtubule stabilization in vivo. However, little is known about the precise microtubule-stabilizing function of MAP6 in neurons.

Here, we demonstrate that depletion of MAP6 induces an increase in dynamic microtubules, accompanied by a decrease of detyrosinated tubulin levels and a higher fluorescence recovery of tubulin after photobleaching in axons, altogether pointing to MAP6 as microtubule stabilizer in neurons. Previous work showed that MAP6 associates preferentially with microtubules containing low levels of tyrosinated tubulin and this interaction is independent of microtubule polyglutamylation (Bonnet et al., 2002; Slaughter and Black, 2003). Consistently, we found that MAP6 binds a specific subset of stable (acetylated and detyrosinated) microtubules. It is tempting to speculate that MAP6 binding induces axonal microtubule stabilization, although we cannot rule out the possibility that MAP6 recognizes stable microtubules and acts to further increase their stability.

While we provide evidence for MAP6-dependent mechanism of microtubule stabilization, it is probable that parallel mechanisms exist in order to organize and stabilize microtubules during axon formation (DiTella et al., 1996; Teng et al., 2001). Other MAPs, such as CAMSAP2 and TRIM46, have been recently shown to mediate microtubule organization by stabilizing non-centrosomal microtubules and forming uniform microtubule arrays before the formation of Tau-positive axons (van Beuningen et al., 2015; Yau et al., 2014). It is plausible that MAP6 may further promote microtubule stabilization of bundles formed by CAMSAP2 and TRIM46. In the more distal part of the axon, microtubules may be stabilized by other MAPs, such as MAP1B or Tau. Furthermore, we found that MAP6 promotes KIF5B-dependent movement and drives efficient mitochondria transport into the axon. As it has been shown for other MAPs, MAP6 could act as a cofactor required for KIF5B-dependent transport or recruit motor proteins to the microtubule (Barlan et al., 2013; Sung et al., 2008). Another possibility is that the binding of MAP6 to axonal microtubules induces conformational changes that promote KIF5B-driven movement into the axon (Tokuraku et al., 2007). Regardless of the precise regulatory mechanism, we show that MAP6 stimulates cargo transport into the developing axon. Interestingly, other MAPs like MAP2 have recently been shown to control cargo trafficking by inhibiting KIF5B motor activity (Gumy et al., 2017).

Palmitoylation Is a Mechanism to Target Proteins to the Axonal Compartment

Two different mechanisms have been proposed to mediate compartment-specific localization of proteins in neurons: selective sorting and selective retention. Whereas some of the axonal or dendritic components are specifically sorted into their final destination, others are transported to both axons and dendrites and are selectively retained in the correct compartment. Palmitoylation has been shown to mediate the localization of neuronal proteins, such as PSD-95, GAP-43, or GAD-65. Interestingly, cycles of palmitoylation and depalmitoylation not only control the localization, but also the activity of palmitoylated proteins,

(E) GFP mean intensity in axons and dendrites of 2DIV hippocampal neurons expressing MAP6-FL, MAP6-GGG, and the different MAP6 domains (n = 15–33 neurons; Kruskal-Wallis test followed by a Dunn's multiple comparison test).
(F) PI for the different constructs in 2DIV hippocampal neurons (n = 22–33 neurons; Kruskal-Wallis test followed by a Dunn's multiple comparison test).
(G) Representative images of 2DIV hippocampal neurons transfected with NPY-GFP and stained for MAP6.
(H) Axon/dendrite ratio quantification of the number of NPY-positive secretory vesicles in control situation (GFP) and neurons transfected with MAP6-shRNA or MAP6-GFP (n = 21–28 neurons; Kruskal-Wallis test followed by a Dunn's multiple comparison test).
(I) Representative stills, zooms, and kymographs of proximal and distal axons from N-terminal domain and NPY-GFP transfected neurons (2DIV).
Graphs represent mean ± SEM in (E), (F), and (H). Scale bar represents 20 μm in (B), (C), (D), and (G) and 5 μm in (I) and zoom in (B), (C), and (D). See also Figure S5.

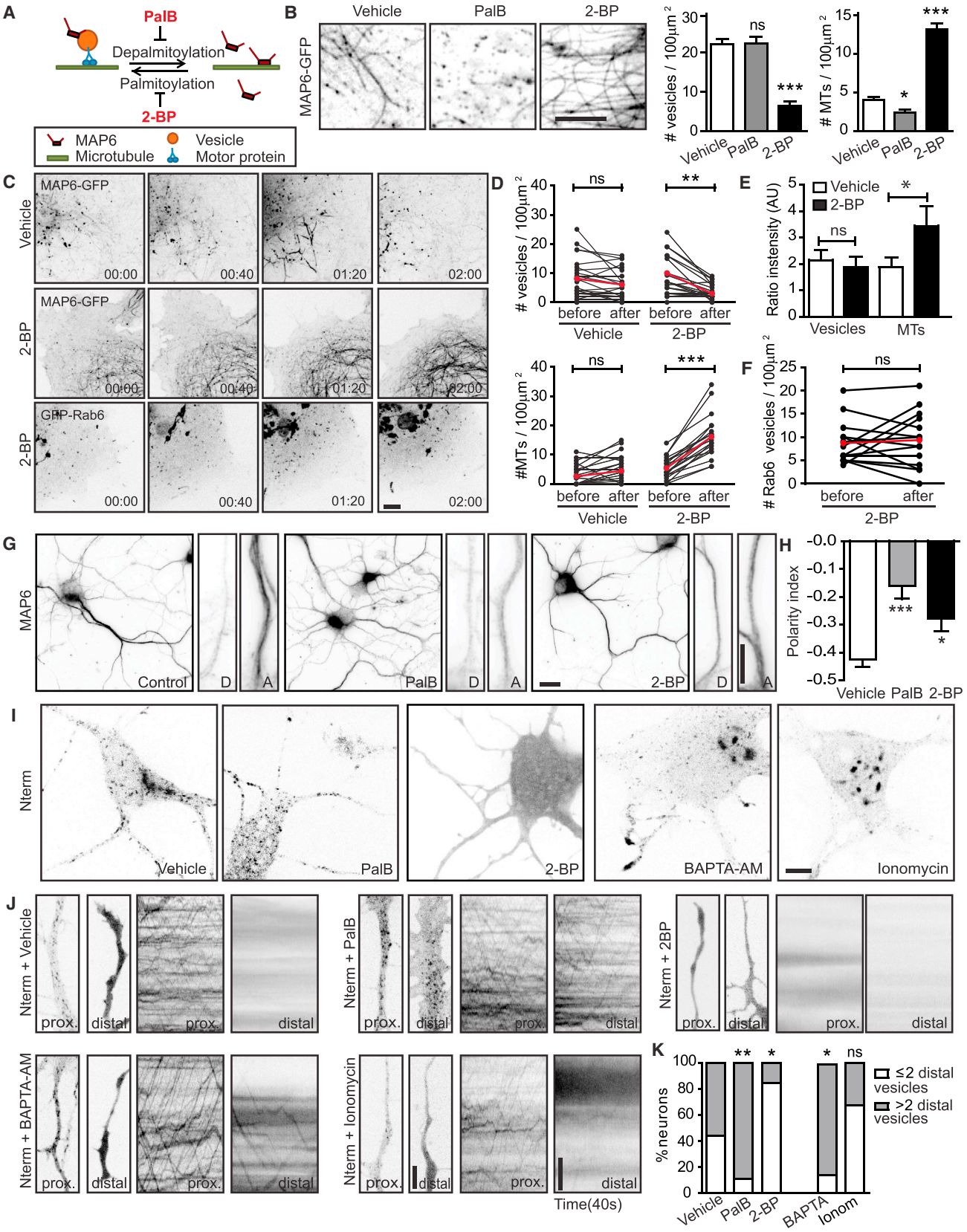

(legend on next page)

regulating processes like the establishment of axon-dendrite polarity or axon growth, guidance, and maintenance (Fukata and Fukata, 2010; Holland and Thomas, 2017). Taken together, results we present here lead us to the conclusion that palmitoylation/depalmitoylation cycles act as a novel mechanism to polarize MAPs neurons.

Model for Controlling MAP6 Membrane-Microtubule Shuttling in Axons

Palmitoylation at the N-terminal region of MAP6 targets the protein to Golgi compartments (Gory-Fauré et al., 2006, 2014). However, the relevance of this lipid modification remained unknown. The absence of the N-terminal domain in MAP6 isoforms present in fibroblasts, astrocytes, and oligodendrocytes (A-, O-, and F-MAP6) suggests that MAP6 palmitoylation may be a unique neuronal feature (Denarier et al., 1998; Galiano et al., 2004). In this study, we show that protein palmitoylation is required for anchoring MAP6 to vesicles and that local depalmitoylation and microtubule binding causes the specific retention of MAP6 in the axon. Interestingly, the same family of α/β Hydrolase domain-containing protein 17 depalmitoylating enzymes involved in PSD-95 and N-Ras depalmitoylation (Lin and Conibear, 2015; Yokoi et al., 2016) control MAP6 palmitoylation, regulating its localization in membranes and microtubules, and its enrichment in axons. Furthermore, previous works have already proposed calcium as a regulatory mechanism of palmitoylation cycles (El-Husseini et al., 2002; Fivaz and Meyer, 2005; Yeh et al., 1999; Zhang et al., 2014). Here, we show that calcium regulates the localization of MAP6 at vesicles, suggesting that MAP6 de-/palmitoylation may be regulated by calcium flux in axons. However, additional studies are needed to elucidate the processes controlling axonal MAP6 depalmitoylation.

We propose a model in which palmitoylated-MAP6 bound to secretory vesicles establishes the initial transport from Golgi to dendrites and axons. Once deplamitoylated MAP6 deattaches from the vesicles, it accumulates in the axon. Regardless of the precise regulatory mechanism, after depalmitoylation, the vesicle-unbound state of MAP6 recognizes a specific subset of microtubules to promote axonal microtubule stabilization. Microtubule stabilization and/or axon-enriched MAP6 may promote delivery of cargo vesicles to the axon or even certain polarity factors that directly contribute to axonal maturation. Our current findings also provide new molecular targets to investigate defects in the polarized sorting machinery in neurodevelopmental disease models.

STAR★METHODS

Detailed methods are provided in the online version of this paper and include the following:

- KEY RESOURCES TABLE
- CONTACT FOR REAGENT AND RESOURCE SHARING
- EXPERIMENTAL MODEL AND SUBJECT DETAILS
  - Animals
  - Primary neuronal cultures and transfection
  - Heterologous cell culture and transfection
  - In utero electroporation
- METHOD DETAILS
  - DNA and shRNA Constructs
  - Antibodies and reagents
  - Immunoblotting
  - Immunofluorescence staining and imaging
  - Live-cell imaging
  - Fluorescence recovery after photobleaching
  - Drug treatments
  - Acyl Rac Assay
  - Inducible cargo trafficking assay
  - Image analysis and quantification
- QUANTIFICATION AND STATISTICAL ANALYSIS

SUPPLEMENTAL INFORMATION

Supplemental Information includes five figures and three movies and can be found with this article online at http://dx.doi.org/10.1016/j.neuron.2017.04.042.

Figure 7. Palmitoylation Cycles Regulate MAP6 Localization and Polarization

(A) Schematic diagram of the model proposed for the action of PalB and 2BP in MAP6 and its binding to vesicles and microtubules.
(B) Representative images and quantifications from COS-7 cells transfected with MAP6-GFP and treated with vehicle control (DMSO), PalB, and 2-BP (n = 42–95 cells; Kruskal-Wallis test followed by a Dunn's multiple comparison test).
(C) Representative stills from MAP6-GFP and GFP-Rab6 time-lapse recordings of COS-7 cells treated with DMSO or 2-BP for 2 hr.
(D) Number of MAP6-positive vesicles and microtubules before and after 2 hr imaging in control and 2-BP treatments (n = 19–24 cells; two-ways ANOVA followed by Bonferroni post-test).
(E) Ratio of the intensity of MAP6-positive vesicles and microtubules before and after 2 hr treatment in control and 2-BP treatments (n = 14 cells; Wilcoxon signed-rank test).
(F) Number of Rab6-positive vesicles before and after 2 hr treatment with 2-BP (n = 19–24 cells; Mann-Whitney U test).
(G) Representative images of DIV2 neurons treated with control DMSO, PalB, and 2-BP for 4 hr and stained for MAP6. Zooms of dendrites (D) and proximal axons (A) are also shown.
(H) PI of MAP6 from DIV2 hippocampal neurons treated with DMSO, PalB, or 2-BP for 4 hr (n = 42–58 neurons; one-way ANOVA followed by a Tukey's multiple comparison test).
(I) Representative stills from DIV2 neurons transfected with N-terminal domain of MAP6 and treated with control (DMSO), PalB, 2-BP, BAPTA-AM, and ionomycin for 4–7 hr.
(J) Zooms of proximal and distal parts of axons together with a kymograph of each region.
(K) Percentage of neurons transfected with N-terminal domain and treated with the different drugs presenting >2 or ≤2 GFP-positive vesicles in the distal part of the axon (n = 24–46 neurons; Fisher's exact test with Bonferroni correction).
Graphs represent mean ± SEM in (B), (E), and (H). Scale bar represents 20 μm in (G), 10 μm in zooms in (G), and 5 μm in (B), (C), (I), and (J). See also Figure S5.

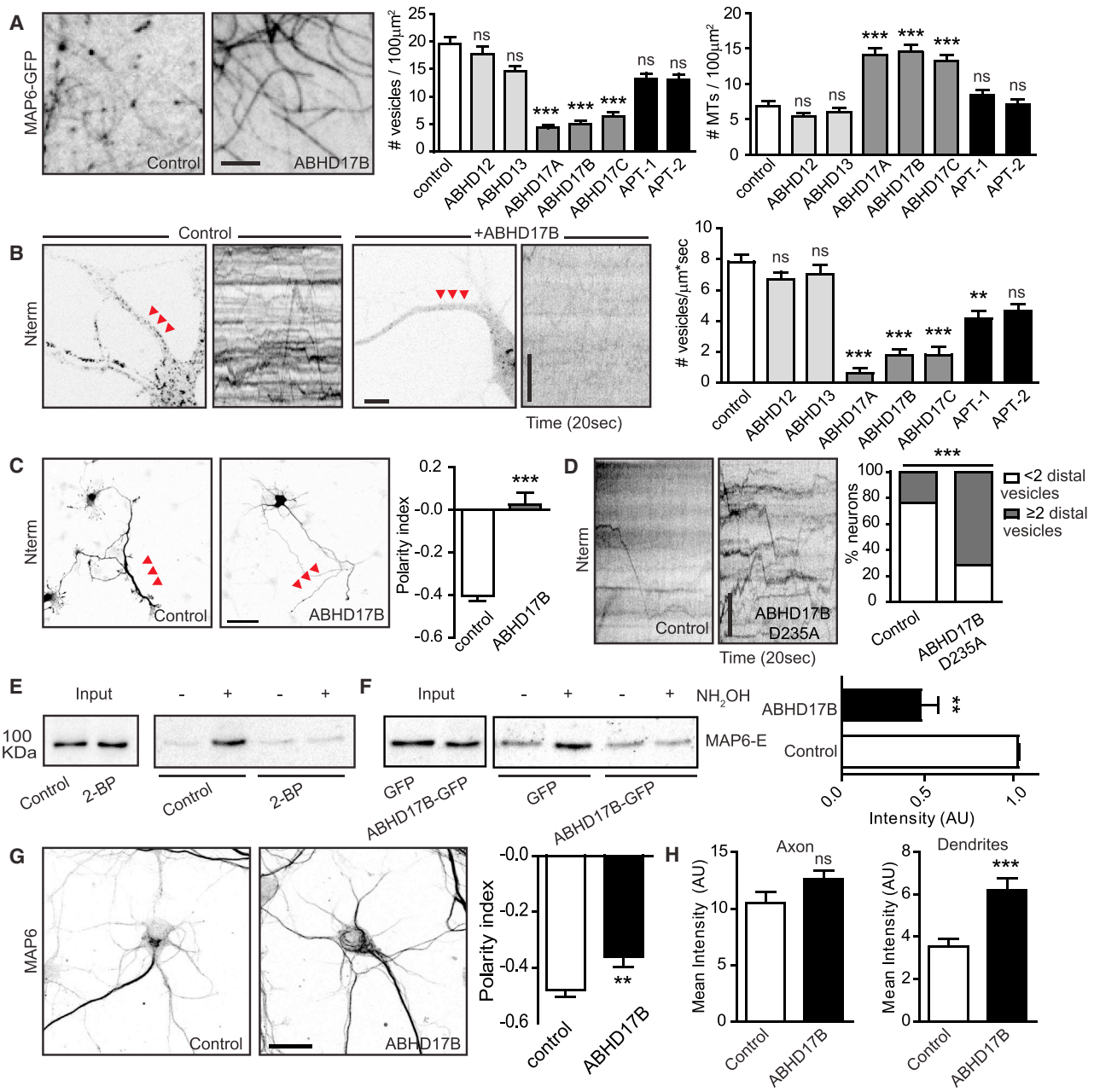

Figure 8. ABHD17B Depalmitoylating Enzyme Controls MAP6 Palmitoylation and Mediates in Its Localization and Polarization

(A) Representative images and quantifications of MAP6-positive vesicles and microtubules from COS-7 cells co-transfected with MAP6-GFP and indicated depalmitoylating enzyme (n = 18–27 cells; Kruskal-Wallis test followed by a Dunn's multiple comparison test).

(B) Representative stills and kymographs from proximal axons from DIV2 neurons co-transfected with the N-terminal domain of MAP6 together with a plasmid control or the depalmitoylating enzyme ABHD17B. On the right, number of MAP6-positive vesicles present in proximal axons of neurons co-transfected with the N-terminal domain of MAP6 and different depalmitoylating enzymes (n = 43–49 neurons; Kruskal-Wallis test followed by a Dunn's multiple comparison test).

(C) Representative images and PI of the N-terminal domain of MAP6 in DIV2 neurons co-transfected with the N-terminal domain together with a plasmid control or ABHD17B (n = 24–28 neurons; unpaired t test). Red arrowheads point to axons in (B) and (C).

(D) Representative kymographs from neurons co-transfected with N-terminal domain of MAP6 together with a plasmid control or the ABHD17B mutant construct ABHD17B D235A. On the right, percentage of neurons presenting >2 or ≤2 GFP-positive vesicles in the distal part of the axon (n = 32–34 neurons; Fisher's exact test).

(E) Representative western blots of cortical neurons (DIV2) treated with control vehicle (DMSO) or 2-BP, subjected to acyl-RAC and analyzed by immunoblotting for MAP6.

(F) Representative western blots and quantifications of cortical neurons (DIV2) nucleofected with a plasmid control (GFP) or ABHD17B, subjected to acyl-RAC and analyzed by immunoblotting for MAP6 (n = 3 experiments; unpaired t test).

(legend continued on next page)

AUTHOR CONTRIBUTIONS

E.T. designed and performed experiments, analyzed data, and wrote the manuscript; Y.A. performed the in utero surgery procedure; M.F. provided critical reagents and gave advice on palmitoylation experiments; R.J.P. supervised in utero experiments; L.C.K. gave advice and edited the manuscript; C.C.H. supervised the research, coordinated the study, and wrote the manuscript.

ACKNOWLEDGMENTS

We thank Prof. Dr. Dieter Edbauer and Dr. Annie Andrieux for sharing MAP6 constructs and antibodies. We thank Dr. Norihiko Yokoi for performing initial palmitoylation experiments and Dr. Amélie Fréal and Dr. Gabriela Plucińska for their in-depth discussion. This work was supported by the Netherlands Organization for Scientific Research (NWO-ALW-VICI, C.C.H. and R.J.P.), the Foundation for Fundamental Research on Matter ([FOM] C.C.H.), which is part of the NWO, the Netherlands Organization for Health Research and Development (ZonMW-TOP, C.C.H.), the European Research Council (ERC) (ERC-consolidator, C.C.H.). E.T. received support by the Spanish Education Ministry and an FP7 European Union Marie Curie postdoctoral fellowship.

Received: July 20, 2016
Revised: February 19, 2017
Accepted: April 27, 2017
Published: May 17, 2017

REFERENCES

Andrieux, A., Salin, P.A., Vernet, M., Kujala, P., Baratier, J., Gory-Fauré, S., Bosc, C., Pointu, H., Proietto, D., Schweitzer, A., et al. (2002). The suppression of brain cold-stable microtubules in mice induces synaptic defects associated with neuroleptic-sensitive behavioral disorders. Genes Dev. *16*, 2350–2364.

Arimura, N., and Kaibuchi, K. (2007). Neuronal polarity: from extracellular signals to intracellular mechanisms. Nat. Rev. Neurosci. *8*, 194–205.

Baas, P.W., and Lin, S. (2011). Hooks and comets: The story of microtubule polarity orientation in the neuron. Dev. Neurobiol. *71*, 403–418.

Baas, P.W., Slaughter, T., Brown, A., and Black, M.M. (1991). Microtubule dynamics in axons and dendrites. J. Neurosci. Res. *30*, 134–153.

Barlan, K., Lu, W., and Gelfand, V.I. (2013). The microtubule-binding protein ensconsin is an essential cofactor of kinesin-1. Curr. Biol. *23*, 317–322.

Bolte, S., and Cordelières, F.P. (2006). A guided tour into subcellular colocalization analysis in light microscopy. J. Microsc. *224*, 213–232.

Bonnet, C., Denarier, E., Bosc, C., Lazereg, S., Denoulet, P., and Larcher, J.C. (2002). Interaction of STOP with neuronal tubulin is independent of polyglutamylation. Biochem. Biophys. Res. Commun. *297*, 787–793.

Bosc, C., Cronk, J.D., Pirollet, F., Watterson, D.M., Haiech, J., Job, D., and Margolis, R.L. (1996). Cloning, expression, and properties of the microtubule-stabilizing protein STOP. Proc. Natl. Acad. Sci. USA *93*, 2125–2130.

Brummelkamp, T.R., Bernards, R., and Agami, R. (2002). A system for stable expression of short interfering RNAs in mammalian cells. Science *296*, 550–553.

Cai, D., McEwen, D.P., Martens, J.R., Meyhofer, E., and Verhey, K.J. (2009). Single molecule imaging reveals differences in microtubule track selection between Kinesin motors. PLoS Biol. *7*, e1000216.

Conde, C., and Cáceres, A. (2009). Microtubule assembly, organization and dynamics in axons and dendrites. Nat. Rev. Neurosci. *10*, 319–332.

Daoust, A., Bohic, S., Saoudi, Y., Debacker, C., Gory-Fauré, S., Andrieux, A., Barbier, E.L., and Deloulme, J.C. (2014). Neuronal transport defects of the MAP6 KO mouse - a model of schizophrenia - and alleviation by Epothilone D treatment, as observed using MEMRI. Neuroimage *96*, 133–142.

Dawson, H.N., Ferreira, A., Eyster, M.V., Ghoshal, N., Binder, L.I., and Vitek, M.P. (2001). Inhibition of neuronal maturation in primary hippocampal neurons from tau deficient mice. J. Cell Sci. *114*, 1179–1187.

Deloulme, J.C., Gory-Fauré, S., Mauconduit, F., Chauvet, S., Jonckheere, J., Boulan, B., Mire, E., Xue, J., Jany, M., Maucler, C., et al. (2015). Microtubule-associated protein 6 mediates neuronal connectivity through Semaphorin 3E-dependent signalling for axonal growth. Nat. Commun. *6*, 7246.

Denarier, E., Fourest-Lieuvin, A., Bosc, C., Pirollet, F., Chapel, A., Margolis, R.L., and Job, D. (1998). Nonneuronal isoforms of STOP protein are responsible for microtubule cold stability in mammalian fibroblasts. Proc. Natl. Acad. Sci. USA *95*, 6055–6060.

DiTella, M.C., Feiguin, F., Carri, N., Kosik, K.S., and Cáceres, A. (1996). MAP-1B/TAU functional redundancy during laminin-enhanced axonal growth. J. Cell Sci. *109*, 467–477.

el-Husseini, Ael.-D., and Bredt, D.S. (2002). Protein palmitoylation: a regulator of neuronal development and function. Nat. Rev. Neurosci. *3*, 791–802.

El-Husseini, Ael.-D., Schnell, E., Dakoji, S., Sweeney, N., Zhou, Q., Prange, O., Gauthier-Campbell, C., Aguilera-Moreno, A., Nicoll, R.A., and Bredt, D.S. (2002). Synaptic strength regulated by palmitate cycling on PSD-95. Cell *108*, 849–863.

Fivaz, M., and Meyer, T. (2005). Reversible intracellular translocation of KRas but not HRas in hippocampal neurons regulated by Ca2+/calmodulin. J. Cell Biol. *170*, 429–441.

Forrester, M.T., Hess, D.T., Thompson, J.W., Hultman, R., Moseley, M.A., Stamler, J.S., and Casey, P.J. (2011). Site-specific analysis of protein S-acylation by resin-assisted capture. J. Lipid Res. *52*, 393–398.

Fournet, V., de Lavilléon, G., Schweitzer, A., Giros, B., Andrieux, A., and Martres, M.P. (2012). Both chronic treatments by epothilone D and fluoxetine increase the short-term memory and differentially alter the mood status of STOP/MAP6 KO mice. J. Neurochem. *123*, 982–996.

Fukata, Y., and Fukata, M. (2010). Protein palmitoylation in neuronal development and synaptic plasticity. Nat. Rev. Neurosci. *11*, 161–175.

Galiano, M.R., Bosc, C., Schweitzer, A., Andrieux, A., Job, D., and Hallak, M.E. (2004). Astrocytes and oligodendrocytes express different STOP protein isoforms. J. Neurosci. Res. *78*, 329–337.

Garner, C.C., Tucker, R.P., and Matus, A. (1988). Selective localization of messenger RNA for cytoskeletal protein MAP2 in dendrites. Nature *336*, 674–677.

Gomis-Rüth, S., Wierenga, C.J., and Bradke, F. (2008). Plasticity of polarization: changing dendrites into axons in neurons integrated in neuronal circuits. Curr. Biol. *18*, 992–1000.

Gory-Fauré, S., Windscheid, V., Bosc, C., Peris, L., Proietto, D., Franck, R., Denarier, E., Job, D., and Andrieux, A. (2006). STOP-like protein 21 is a novel member of the STOP family, revealing a Golgi localization of STOP proteins. J. Biol. Chem. *281*, 28387–28396.

Gory-Fauré, S., Windscheid, V., Brocard, J., Montessuit, S., Tsutsumi, R., Denarier, E., Fukata, Y., Bosc, C., Delaroche, J., Collomb, N., et al. (2014). Non-microtubular localizations of microtubule-associated protein 6 (MAP6). PLoS ONE *9*, e114905.

Grigoriev, I., Splinter, D., Keijzer, N., Wulf, P.S., Demmers, J., Ohtsuka, T., Modesti, M., Maly, I.V., Grosveld, F., Hoogenraad, C.C., and Akhmanova, A. (2007). Rab6 regulates transport and targeting of exocytotic carriers. Dev. Cell *13*, 305–314.

Guillaud, L., Bosc, C., Fourest-Lieuvin, A., Denarier, E., Pirollet, F., Lafanechère, L., and Job, D. (1998). STOP proteins are responsible for the high degree of microtubule stabilization observed in neuronal cells. J. Cell Biol. *142*, 167–179.

(G) Representative images and PI of DIV2 neurons transfected with a plasmid control or ABHD17B and stained for MAP6 (n = 34–36 neurons; unpaired t test). (H) MAP6 mean intensity quantification in axons and dendrites of DIV2 neurons transfected with a plasmid control or ABHD17B (n = 34–36 neurons; unpaired t test).

Graphs represent mean ± SEM in (A), (B), (C), (F), (G), and (H). Scale bar represents 20 μm in (C) and (G) and 5 μm in (A), (B), and (D). See also Figure S5.

Gumy, L.F., Katrukha, E.A., Grigoriev, I., Jaarsma, D., Kapitein, L.C., Akhmanova, A., and Hoogenraad, C.C. (2017). MAP2 defines a pre-axonal filtering zone to regulate KIF1- versus KIF5-dependent cargo transport in sensory neurons. Neuron *94*, 347–362.e347.

Hand, R., Bortone, D., Mattar, P., Nguyen, L., Heng, J.I., Guerrier, S., Boutt, E., Peters, E., Barnes, A.P., Parras, C., et al. (2005). Phosphorylation of Neurogenin2 specifies the migration properties and the dendritic morphology of pyramidal neurons in the neocortex. Neuron *48*, 45–62.

Hirokawa, N., Funakoshi, T., Sato-Harada, R., and Kanai, Y. (1996). Selective stabilization of tau in axons and microtubule-associated protein 2C in cell bodies and dendrites contributes to polarized localization of cytoskeletal proteins in mature neurons. J. Cell Biol. *132*, 667–679.

Holland, S.M., and Thomas, G.M. (2017). Roles of palmitoylation in axon growth, degeneration and regeneration. J. Neurosci. Res. Published online February 2, 2017. http://dx.doi.org/10.1002/jnr.24003.

Honnappa, S., Gouveia, S.M., Weisbrich, A., Damberger, F.F., Bhavesh, N.S., Jawhari, H., Grigoriev, I., van Rijssel, F.J., Buey, R.M., Lawera, A., et al. (2009). An EB1-binding motif acts as a microtubule tip localization signal. Cell *138*, 366–376.

Hoogenraad, C.C., and Bradke, F. (2009). Control of neuronal polarity and plasticity–a renaissance for microtubules? Trends Cell Biol. *19*, 669–676.

Kanai, Y., and Hirokawa, N. (1995). Sorting mechanisms of tau and MAP2 in neurons: suppressed axonal transit of MAP2 and locally regulated microtubule binding. Neuron *14*, 421–432.

Kapitein, L.C., and Hoogenraad, C.C. (2015). Building the Neuronal Microtubule Cytoskeleton. Neuron *87*, 492–506.

Kapitein, L.C., Schlager, M.A., Kuijpers, M., Wulf, P.S., van Spronsen, M., MacKintosh, F.C., and Hoogenraad, C.C. (2010). Mixed microtubules steer dynein-driven cargo transport into dendrites. Curr. Biol. *20*, 290–299.

Kollins, K.M., Bell, R.L., Butts, M., and Withers, G.S. (2009). Dendrites differ from axons in patterns of microtubule stability and polymerization during development. Neural Dev. *4*, 26.

Leugers, C.J., and Lee, G. (2010). Tau potentiates nerve growth factor-induced mitogen-activated protein kinase signaling and neurite initiation without a requirement for microtubule binding. J. Biol. Chem. *285*, 19125–19134.

Li, X., Kumar, Y., Zempel, H., Mandelkow, E.M., Biernat, J., and Mandelkow, E. (2011). Novel diffusion barrier for axonal retention of Tau in neurons and its failure in neurodegeneration. EMBO J. *30*, 4825–4837.

Lin, D.T., and Conibear, E. (2015). ABHD17 proteins are novel protein depalmitoylases that regulate N-Ras palmitate turnover and subcellular localization. eLife *4*, e11306.

Lu, M., and Kosik, K.S. (2001). Competition for microtubule-binding with dual expression of tau missense and splice isoforms. Mol. Biol. Cell *12*, 171–184.

Meijering, E., Jacob, M., Sarria, J.C., Steiner, P., Hirling, H., and Unser, M. (2004). Design and validation of a tool for neurite tracing and analysis in fluorescence microscopy images. Cytometry A *58*, 167–176.

Nakata, T., and Hirokawa, N. (2003). Microtubules provide directional cues for polarized axonal transport through interaction with kinesin motor head. J. Cell Biol. *162*, 1045–1055.

Okabe, S., and Hirokawa, N. (1989). Rapid turnover of microtubule-associated protein MAP2 in the axon revealed by microinjection of biotinylated MAP2 into cultured neurons. Proc. Natl. Acad. Sci. USA *86*, 4127–4131.

Poulain, F.E., and Sobel, A. (2010). The microtubule network and neuronal morphogenesis: Dynamic and coordinated orchestration through multiple players. Mol. Cell. Neurosci. *43*, 15–32.

Rocks, O., Peyker, A., Kahms, M., Verveer, P.J., Koerner, C., Lumbierres, M., Kuhlmann, J., Waldmann, H., Wittinghofer, A., and Bastiaens, P.I. (2005). An acylation cycle regulates localization and activity of palmitoylated Ras isoforms. Science *307*, 1746–1752.

Schlager, M.A., Kapitein, L.C., Grigoriev, I., Burzynski, G.M., Wulf, P.S., Keijzer, N., de Graaff, E., Fukuda, M., Shepherd, I.T., Akhmanova, A., and Hoogenraad, C.C. (2010). Pericentrosomal targeting of Rab6 secretory vesicles by Bicaudal-D-related protein 1 (BICDR-1) regulates neuritogenesis. EMBO J. *29*, 1637–1651.

Schlager, M.A., Serra-Marques, A., Grigoriev, I., Gumy, L.F., Esteves da Silva, M., Wulf, P.S., Akhmanova, A., and Hoogenraad, C.C. (2014). Bicaudal d family adaptor proteins control the velocity of Dynein-based movements. Cell Rep. *8*, 1248–1256.

Schwenk, B.M., Lang, C.M., Hogl, S., Tahirovic, S., Orozco, D., Rentzsch, K., Lichtenthaler, S.F., Hoogenraad, C.C., Capell, A., Haass, C., and Edbauer, D. (2014). The FTLD risk factor TMEM106B and MAP6 control dendritic trafficking of lysosomes. EMBO J. *33*, 450–467.

Slaughter, T., and Black, M.M. (2003). STOP (stable-tubule-only-polypeptide) is preferentially associated with the stable domain of axonal microtubules. J. Neurocytol. *32*, 399–413.

Sung, H.H., Telley, I.A., Papadaki, P., Ephrussi, A., Surrey, T., and Rørth, P. (2008). Drosophila ensconsin promotes productive recruitment of Kinesin-1 to microtubules. Dev. Cell *15*, 866–876.

Szebenyi, G., Bollati, F., Bisbal, M., Sheridan, S., Faas, L., Wray, R., Haferkamp, S., Nguyen, S., Caceres, A., and Brady, S.T. (2005). Activity-driven dendritic remodeling requires microtubule-associated protein 1A. Curr. Biol. *15*, 1820–1826.

Takei, Y., Teng, J., Harada, A., and Hirokawa, N. (2000). Defects in axonal elongation and neuronal migration in mice with disrupted tau and map1b genes. J. Cell Biol. *150*, 989–1000.

Teng, J., Takei, Y., Harada, A., Nakata, T., Chen, J., and Hirokawa, N. (2001). Synergistic effects of MAP2 and MAP1B knockout in neuronal migration, dendritic outgrowth, and microtubule organization. J. Cell Biol. *155*, 65–76.

Tokuraku, K., Noguchi, T.Q., Nishie, M., Matsushima, K., and Kotani, S. (2007). An isoform of microtubule-associated protein 4 inhibits kinesin-driven microtubule gliding. J. Biochem. *141*, 585–591.

Tortosa, E., Galjart, N., Avila, J., and Sayas, C.L. (2013). MAP1B regulates microtubule dynamics by sequestering EB1/3 in the cytosol of developing neuronal cells. EMBO J. *32*, 1293–1306.

van Beuningen, S.F., and Hoogenraad, C.C. (2016). Neuronal polarity: remodeling microtubule organization. Curr. Opin. Neurobiol. *39*, 1–7.

van Beuningen, S.F., Will, L., Harterink, M., Chazeau, A., van Battum, E.Y., Frias, C.P., Franker, M.A., Katrukha, E.A., Stucchi, R., Vocking, K., et al. (2015). TRIM46 Controls Neuronal Polarity and Axon Specification by Driving the Formation of Parallel Microtubule Arrays. Neuron *88*, 1208–1226.

van Spronsen, M., Mikhaylova, M., Lipka, J., Schlager, M.A., van den Heuvel, D.J., Kuijpers, M., Wulf, P.S., Keijzer, N., Demmers, J., Kapitein, L.C., et al. (2013). TRAK/Milton motor-adaptor proteins steer mitochondrial trafficking to axons and dendrites. Neuron *77*, 485–502.

Witte, H., Neukirchen, D., and Bradke, F. (2008). Microtubule stabilization specifies initial neuronal polarization. J. Cell Biol. *180*, 619–632.

Yau, K.W., van Beuningen, S.F., Cunha-Ferreira, I., Cloin, B.M., van Battum, E.Y., Will, L., Schätzle, P., Tas, R.P., van Krugten, J., Katrukha, E.A., et al. (2014). Microtubule minus-end binding protein CAMSAP2 controls axon specification and dendrite development. Neuron *82*, 1058–1073.

Yau, K.W., Schätzle, P., Tortosa, E., Pagès, S., Holtmaat, A., Kapitein, L.C., and Hoogenraad, C.C. (2016). Dendrites in vitro and in vivo contain microtubules of opposite polarity and axon formation correlates with uniform plus-end-out microtubule orientation. J. Neurosci. *36*, 1071–1085.

Yeh, D.C., Duncan, J.A., Yamashita, S., and Michel, T. (1999). Depalmitoylation of endothelial nitric-oxide synthase by acyl-protein thioesterase 1 is potentiated by Ca(2+)-calmodulin. J. Biol. Chem. *274*, 33148–33154.

Yokoi, N., Fukata, Y., Sekiya, A., Murakami, T., Kobayashi, K., and Fukata, M. (2016). Identification of PSD-95 Depalmitoylating Enzymes. J. Neurosci. *36*, 6431–6444.

Zhang, Y., Matt, L., Patriarchi, T., Malik, Z.A., Chowdhury, D., Park, D.K., Renieri, A., Ames, J.B., and Hell, J.W. (2014). Capping of the N-terminus of PSD-95 by calmodulin triggers its postsynaptic release. EMBO J. *33*, 1341–1353.

STAR★METHODS

KEY RESOURCES TABLE

REAGENT or RESOURCE	SOURCE	IDENTIFIER
Antibodies		
rabbit anti-MAP6	Kind gift from Dr. Andrieux	N/A
goat anti-MAP1A	Santa Cruz Biotechnology	sc8969, RRID: AB_649150
goat anti-MAP1B	Santa Cruz Biotechnology	sc8970, RRID: AB_649156
chicken anti-MAP2	Abcam	ab5392, RRID: AB_2138153
mouse anti-MAP2 (clone HM-2)	Sigma-Aldrich	M9942, RRID: AB_477256
mouse anti- dephosphorylated Tau (clone PC1C6)	Chemicon	MAB3420, RRID: AB_94855
rabbit anti-TRIM46	From C.C. Hoogenraad, van Beuningen et al., 2015	N/A
mouse anti-pan-Na_v (clone K58/35)	Sigma-Aldrich	S8809, RRID: AB_477552
rabbit anti-βIVSpectrin	Kind gift from Dr. M. Rasband	N/A
mouse anti-EB1 (clone 5/EB1)	BD Transduction Laboratories	610535, RRID: AB_397892
rabbit anti-GFP	MBL	598, RRID: AB_591819
rabbit anti-GFP	Abcam	ab290, RRID: AB_303395
mouse anti-GFP	Roche	11814460001, RRID: AB_390913
rabbit anti-β-III tubulin	Covance	PRB-435P, RRID: AB_291637
mouse anti-α-tubulin (clone B-5-1-2)	Sigma-Aldrich	T-5168, RRID: AB_477579
rabbit anti-detyrosinated tubulin	Millipore	AB3201, RRID: AB_177350
mouse anti-acetylated tubulin	Sigma-Aldrich	T7451, RRID: AB_609894
rat anti-tubulin-tyrosinated (YL1/2,)	Abcam	ab6160, RRID: AB_305328
chicken anti-Neurofilament-200kDa	Abcam	ab72996, RRID: AB_2149618
mouse anti-actin	Millipore	MAB1501R, RRID: AB_2223041
mouse anti-GM130	BD Transduction Laboratories	610823, RRID: AB_398142
mouse anti-Rab6	Kind gift from A. Barnekow	N/A
mouse anti-SCG10 (clone L5/1)	NeuroMab	75-063, RRID: AB_2302747
mouse anti-LAMP1 (clone LY1C6)	Enzo Life Sciences	ADI-VAM-EN001, RRID: AB_2038958
mouse anti-Rab3	BD Transduction Laboratories	610379, RRID: AB_397762
anti-mouse Alexa488	Life Technologies	A11029, RRID: AB_2534088
anti-rabbit Alexa488	Life Technologies	A11034, RRID: AB_2576217
anti-rat Alexa488	Life Technologies	A11006, RRID: AB_2534074
anti-goat Alexa488	Life Technologies	A11055, RRID: AB_2534102
anti-mouse Alexa568	Life Technologies	A11031, RRID: AB_144696
anti-rabbit Alexa568	Life Technologies	A11036, RRID: AB_10563566
anti-goat Alexa568	Life Technologies	A11057, RRID: AB_2534104
anti-mouse Alexa647	Life Technologies	A21236, RRID: AB_2535805
anti-rabbit Alexa647	Life Technologies	A21245, RRID: AB_2535813
anti-chicken Alexa647	Life Technologies	A21449, RRID: AB_2535866
anti-mouse Cy3	Jackson ImmunoResearch	715-165-150, RRID: AB_2340813
anti-rabbit Cy3	Jackson ImmunoResearch	711-165-152, RRID: AB_2307443
anti-mouse Cy5	Abcam	ab6563, RRID: AB_955068
anti-rabbit Cy5	Abcam	ab6564, RRID: AB_955061
anti-chicken Dyelight405	Jackson ImmunoResearch	703-475-155, RRID: AB_2340373
anti-mouse anti-HRP	DAKO	P0260, RRID: AB_2636929
anti-rabbit anti-HRP	DAKO	P0399, RRID: AB_2617141

(*Continued on next page*)

Continued

REAGENT or RESOURCE	SOURCE	IDENTIFIER
Chemicals, Peptides, and Recombinant Proteins		
Rapalog	Takara	635057
S-Methyl methanethiosulfonate	Sigma-Aldrich	208795-1G
Thiopropyl–Sepharose 6B	Sigma-Aldrich	T8387-1G
Hydroxylamine hydrochloride 6B (Sigma Aldrich)	Sigma-Aldrich	379921-5G
Palmostatin B	Calbiochem	178501-5MG
2-Bromopalmitate	Sigma-Aldrich	21604-1G
Paclitaxel	Sigma-Aldrich	T7402
Ionomycin	Santa Cruz Biotechnology	sc-3592
BAPTA-AM	Santa Cruz Biotechnology	sc-202488
Fugene6	Promega	E2691
Lipofectamine 2000	Thermofisher	11668019
Vectashield mounting medium	Vectorlabs	H-1000
Critical Commercial Assays		
Rat Neuron Nucleofector kit	Amaxa	VVPG-1003
Experimental Models: Cell Lines		
African Green Monkey SV40-transformed kidney fibroblast (COS-7)	ATCC	CRL-1651
Human Fetal Lung Fibroblast Cells (MRC-5)	ATCC	CCL-171
Experimental Models: Organisms/Strains		
Rat (Wistar)	Janvier	N/A
Mouse (C57BL/6)	Jackson Laboratories	N/A
Oligonucleotides		
Primer: SalI -Nterm domain Forward: tactcgtcgactatggc gtggccgtgca	This paper	N/A
Primer: XbaI-Nterm domain Reverse: gttatctagatcacgcc gggcctgagcc	This paper	N/A
Primer: SalI -MTB domain Forward: ctcgtcgactgactcggt gatgcgacaggac	This paper	N/A
Primer: XbaI-MTB domain Reverse: gcgtctagatcagggctt ggctttgattggtttcac	This paper	N/A
Primer: SalI -Cterminal domain Forward: ttagtcgactcagt acaagcccccagatgacaag	This paper	N/A
Primer: XbaI-Cterminal domain Reverse: ggcgcatcctcta gatcattactctttcgcctcagccag	This paper	N/A
Primer: SalI -Nterm -GGG Forward: atactcgtcgactatggcgt ggccgggcatcactagggccggcggcatcgcccgcttctggaaccagctg	This paper	N/A
Recombinant DNA		
pGW1-GFP	Kapitein et al., 2010	N/A
Tau 4R-GFP	Lu and Kosik, 2001	N/A
MAP6-N-GFP	Kind gift from Dr. Andrieux	N/A
MAP6-E-GFP	Kind gift from Dr. Andrieux	N/A
GFP-MAP6-E	Kind gift from Dr. Andrieux	N/A
ABHD12-FLAG	Yokoi et al., 2016	N/A
ABHD13-FLAG	Yokoi et al., 2016	N/A
ABHD17A-FLAG	Yokoi et al., 2016	N/A
ABHD17B-FLAG	Yokoi et al., 2016	N/A
ABHD17C-FLAG	Yokoi et al., 2016	N/A
APT1 -FLAG	Yokoi et al., 2016	N/A
APT2-FLAG	Yokoi et al., 2016	N/A

(*Continued on next page*)

Continued

REAGENT or RESOURCE	SOURCE	IDENTIFIER
ABHD17B-GFP	Yokoi et al., 2016	N/A
ABHD17B D235A -FLAG	Yokoi et al., 2016	N/A
GFP-MACF43	Honnappa et al., 2009	N/A
NPY-GFP	Schlager et al., 2010	N/A
NPY-RFP	Grigoriev et al., 2007	N/A
mCitrine-Nras	Rocks et al., 2005	N/A
tagRFP-Rab6	Schlager et al., 2014	N/A
mito-dsRed	van Spronsen et al., 2013	N/A
KIF5B(1-807)-GFP	Kapitein et al., 2010	N/A
KIF5B(1-807)-HA-FRB	Kapitein et al., 2010	N/A
PEX3-RFP-FKBP	Kapitein et al., 2010	N/A
β-tubulin-GFP	Kind gift from Dr. P. Schältze and Dr. K. Jiang	N/A
pSuper vector	Brummelkamp et al., 2002	N/A
pSuper-rat MAP1A shRNA #1 shRNA targeting sequence: gctctttcgtcgaagataa	This paper	N/A
pSuper-rat MAP1A shRNA #2	Szebenyi et al., 2005	N/A
pSuper-rat MAP1B shRNA shRNA targeting sequence: gcccaagaaggaagtggct	This paper. Adapted from Tortosa et al., 2013	N/A
pSuper-rat MAP2 shRNA	Kapitein et al., 2010	N/A
pSuper-rat Tau shRNAs	Leugers and Lee, 2010	N/A
pSuper-rat/mouse MAP6 shRNA #1	Schwenk et al., 2014	N/A
pSuper-rat MAP6 shRNA #2	Schwenk et al., 2014	N/A
pSuper-mouse MAP6 #2 shRNA targeting sequence: gatggtgactcgcacggaa	This paper. Adapted from Schwenk et al., 2014	N/A
pSuper-rat MAP6-shRNA #3 shRNA targeting sequence: ccagtaagcccaccacagcggacaa	Kind gift from Dr. Andrieux	N/A
Software and Algorithms		
ImageJ	NIH	https://imagej.nih.gov/ij/
NeuronJ	Meijering et al., 2004	N/A
JACoP plugin	Bolte and Cordelières, 2006	N/A
ComDet	GitHub	https://github.com/ekatrukha/ComDet
Kymoreslicewide	GitHub	https://github.com/ekatrukha/KymoResliceWide

CONTACT FOR REAGENT AND RESOURCE SHARING

Further information and requests for resources and reagents should be directed to and will be fulfilled by the Lead Contact Casper Hoogenraad (c.hoogenraad@uu.nl).

EXPERIMENTAL MODEL AND SUBJECT DETAILS

Animals

All experiments with animals were performed in compliance with the guidelines for the welfare of experimental animals issued by the Government of the Netherlands, and were approved by the Animal Ethical Review Committee (DEC) of Utrecht University.

Primary neuronal cultures and transfection

Primary hippocampal and cortical cultures were prepared from embryonic day 18 rat brains (both genders). Cells were plated on coverslips coated with poly-L-lysine (37.5 μg/mL) and laminin (1.25 μg/mL) at a density of 100,000/well. Neurons were cultured in Neurobasal medium (NB) supplemented with 2% B27 (GIBCO), 0.5 mM glutamine (GIBCO), 15.6 μM glutamate (Sigma), and 1% penicillin/streptomycin (GIBCO) at 37°C in 5% CO_2.

Hippocampal neurons were transfected using Lipofectamine 2000 (Invitrogen). Briefly, DNA (1.8 μg/well, of a 12 wells plate) was mixed with 3.3 μL of Lipofectamine 2000 in 200 μL NB, incubated for 30 min, and then added to the neurons in NB at 37°C in 5% CO_2 for 45 min. Next, neurons were washed with NB and transferred to their original medium at 37°C in 5% CO_2 for 24h (for overexpression) or 72h (for shRNA expression).

Primary cortical neurons (1.3×10^6 cells) were nucleofected with 3 μg of DNA using the Amaxa Rat Neuron Nucleofector kit (Lonza) according to the manufacturer's instructions. Cells were maintained for 3 days (knockdown experiments) or 1 day (other experiments) at 37°C in 5% CO_2 before imaging or fixation.

For immunocytochemistry, cells were fixed for 10 min with paraformaldehyde (4%) or for 5 min with methanol (100%) containing 1mM EGTA at −20°C followed by 5 min paraformaldehyde (4%). Cells with low expression levels of the different constructs were used in all the analysis.

Heterologous cell culture and transfection

African Green Monkey SV40-transformed kidney fibroblast (COS-7) and Human Fetal Lung Fibroblast Cells (MRC-5) cells were from ATCC and cultured in DMEM/Ham's F10 (50%/50%) supplemented with 10% FCS and 1% penicillin/streptomycin at 37°C and 5% CO_2. Cell lines were not authenticated by authors after purchase. Cells were plated in 18mm glass coverslips and transfected with Fugene6 (Promega) according to manufacturer's protocol. Cells with low expression levels of the different constructs were used in all the studies.

In utero electroporation

In utero electroporation was performed as described previously (van Beuningen et al., 2015). Briefly, pregnant female C57BL/6 mice (Jackson Laboratories) were anaesthetized with Isoflurane (induction: 3%–4%, surgery, 1.5%–2%) and injected with 0.05mg/kg buprenorfinhydrochloride in saline at E14.5. The abdominal cavity was opened and uterine horns were exposed under sterile surgical conditions. 1.7 μL DNA mixture containing 0.6 μg/μL pSuper vector or MAP6 shRNAs, and 0.4 μg/μL GFP vector dissolved in MilliQ water with 0.05% Fast Green (Sigma) was injected in the lateral ventricles of the embryos (both males and females) using glass micro-pipettes (Harvard Apparatus) and a PLI-100 Picoinjector (Harvard Apparatus). Brains (motor cortex) were electroporated with gold plated tweezer-electrodes (Fischer Scientific) using an ECM 830 Electro-Square-Porator (Harvard Apparatus) set to three unipolar pulses at 30V (100ms interval and pulse length). Embryos were placed back into the abdomen, and abdominal muscles and skin were sutured separately. Mother mice were awakened by releasing them from Isoflurane. Whole heads of embryos were collected at E17.5 and processed for immunohistochemistry. The percentage of neuronal migration was quantified as described previously (Hand et al., 2005).

METHOD DETAILS

DNA and shRNA Constructs

MAP6 clones were kindly provided by both Dr. Annie Andrieux (Grenoble Institut des Neurosciences) and Prof. Dr. Dieter Edbauer (DZNE-München). All MAP6 expression constructs were generated by a PCR-based strategy and placed in GW1 vector (Kapitein et al., 2010). In palmitoylation-defective MAP6 mutant (MAP6-GGG and N-terminal-GGG) cysteins C5, C10 and C11 were mutated to glycine residues by a PCR-based strategy. C-terminal GFP-tagged MAP6-E isoform was used in most of overexpression experiments, excluding Figures 6B and 6D. In young neurons, although both C-terminal and N-terminal GFP-tagged version of MAP6-E present a polarized distribution, only MAP6-GFP distribution matches nicely with the endogenous MAP6 in proximal axons, where both, endogenous and overexpressed protein, bind microtubules. GFP-MAP6 full length doesn't seem to be so efficient in binding microtubules, therefore it does not accumulate in proximal axons and becomes enriched in more distal regions.

Plasmids for depalmitoylating enzymes ABHD12, 13, 17A/B/C, APT1 and 2, and the ABHD17B mutant construct ABHD17B D235A have been previously described (Yokoi et al., 2016). The following mammalian expression plasmids have been previously described: pSuper vector (Brummelkamp et al., 2002), GFP-Tau 4R (Lu and Kosik, 2001), GFP-MACF43 (Honnappa et al., 2009) which we named GFP-MT+TIP since it is used as a general marker to analyze the dynamics of microtubule growing plus-ends, NPY-GFP (Schlager et al., 2010), mCitrine-Nras (Rocks et al., 2005), NPY-RFP (Grigoriev et al., 2007), tagRFP-Rab6 (Schlager et al., 2014), mito-dsRed (van Spronsen et al., 2013), pGW1-GFP, KIF5B(1-807)-GFP and constructs used for the inducible cargo trafficking assay including KIF5B(1-807)-HA-FRB and PEX3-RFP-FKBP (Kapitein et al., 2010). GW2-BFP was created by inserting BFP into HindIII/AscI sites of a GW2 backbone. β-tubulin-GFP was a kind gift from Dr. P. Schältze and Dr. K. Jiang. The following shRNAs were used in this study: rat/mouse MAP6-shRNA#1 (5′- ggtgcagatcagcgtgaca −3′) and rat MAP6-shRNA#2 (5′-gatggtgactcgcaccgaa-3′) (Schwenk et al., 2014), mouse MAP6 shRNA#2 (5′-gatggtgactcgcacggaa −3′) and rat MAP6-shRNA#3 (5′-ccagtaagcccaccacagcggacaa −3′). MAP1A shRNA #1 (5′- gctctttcgtcgaagataa −3′) and MAP1A shRNA #2 (Szebenyi et al., 2005), MAP1B shRNA (adapted from (Tortosa et al., 2013); 5′-gcccaagaaggaagtggct-3′), MAP2-shRNA (Kapitein et al., 2010) and Tau-shRNA (Leugers and Lee, 2010).

Antibodies and reagents

The following antibodies were used in this study: rabbit anti-MAP6 (kind gift from Dr. Annie Andrieux), goat anti-MAP1A (Santa Cruz Biotechnology, sc8969, RRID: AB_649150), goat anti-MAP1B (Santa Cruz Biotechnology, sc8970, RRID: AB_649156), chicken

anti-MAP2 (Abcam, ab5392, RRID: AB_2138153), mouse anti-MAP2 (clone HM-2; Sigma-Aldrich, M9942, RRID: AB_477256), rabbit anti-β-III tubulin (Covance, PRB-435P, RRID: AB_291637), mouse anti-pan-Na_v (clone K58/35, Sigma, S8809, RRID: AB_477552), rabbit anti-βIVSpectrin (kind gift from Dr. M. Rasband), mouse anti- dephosphorylated Tau (clone PC1C6, Chemicon, MAB3420, RRID: AB_94855), mouse anti-EB1 (clone 5/EB1, BD Transduction Laboratories, 610535, RRID: AB_397892), rabbit anti-GFP (MBL, 598, RRID: AB_591819; Abcam, ab290, RRID: AB_303395), mouse anti-GFP (Roche, 11814460001, RRID: AB_390913), mouse anti-α-tubulin (Sigma-Aldrich, T-5168, RRID: AB_477579), rabbit anti-detyrosinated tubulin (Millipore, AB3201, RRID: AB_177350), mouse anti-acetylated tubulin (Sigma-Aldrich, T7451, RRID: AB_609894), anti-tubulin-tyrosinated (YL1/2, Abcam, ab6160, RRID: AB_305328), anti-TRIM46 (van Beuningen et al., 2015), chicken anti-Neurofilament-200kDa (Abcam, ab72996, RRID: AB_2149618), anti-actin (Millipore, MAB1501R, RRID: AB_2223041), anti-GM130 (BD Transduction Laboratories, 610823, RRID: AB_398142), anti-Rab6 (a gift of A. Barnekow, University of Muenster, Germany), anti-SCG10 (NeuroMab, clone L5/1, 75-063, RRID: AB_2302747), anti-LAMP1 (Enzo Life Sciences, LY1C6, RRID: AB_2038958), anti-Rab3 (BD Transduction Laboratories, 610379, RRID: AB_397762). anti-mouse Alexa488 (Life Technologies, A11029, RRID: AB_2534088), anti-rabbit Alexa488 (Life Technologies, A11034, RRID: AB_2576217), anti-rat Alexa488 (Life Technologies, A11006, RRID: AB_2534074), anti-goat Alexa488 (Life Technologies, A11055, RRID: AB_2534102), anti-mouse Alexa568 (Life Technologies A11031, RRID: AB_144696), anti-rabbit Alexa568 (Life Technologies, A11036, RRID: AB_10563566), anti-goat Alexa568 (Life Technologies, A11057, RRID: AB_2534104), anti-mouse Alexa647 (Life Technologies A21236, RRID: AB_2535805), anti-rabbit Alexa647 (Life Technologies, A21245, RRID: AB_2535813), anti-chicken Alexa647 (Life Technologies A21449, RRID: AB_2535866), anti-mouse Cy3 (Jackson ImmunoResearch, 715-165-150, RRID: AB_2340813), anti-rabbit Cy3, (Jackson ImmunoResearch, 711-165-152, RRID: AB_2307443), anti-mouse Cy5 (Abcam, ab6563, RRID: AB_955068), anti-rabbit Cy5 (Abcam, ab6564, RRID: AB_955061), anti-chicken Dyelight405 (Jackson ImmunoResearch, 703-475-155, RRID: AB_2340373), anti-mouse anti-HRP DAKO (P0260, RRID: AB_2636929), anti-rabbit anti-HRP (DAKO, P0399, RRID: AB_2617141).

Other reagents used in this study were Rapalog (Takara, 635057), S-Methyl methanethiosulfonate (Sigma-Aldrich, 208795-1G), Thiopropyl–Sepharose 6B (Sigma-Aldrich, T8387-1G), Hydroxylamine hydrochloride 6B (Sigma-Aldrich 379921-5G), Palmostatin B (Calbiochem 178501-5MG), 2-Bromopalmitate (Sigma-Aldrich, 21604-1G), Paclitaxel (Sigma-Aldrich, T7402), Ionomycin (Santa Cruz Biotechnology, sc-3592), BAPTA-AM (Santa Cruz Biotechnology, sc-202488), Fugene6 (Promega, E2691), Lipofectamine2000 (Thermofisher, 11668019), Vectashield mounting medium (Vectorlabs, H-1000).

Immunoblotting

Neurons were directly lysed in SDS-page sample buffer containing DTT, boiled for 10 min and subjected to 8% SDS-page followed by blotting on nitrocellulose membranes using a semi-dry blotting setup. Membranes were blocked for 1 hr in 5% bovine serum albumin in PBS/0.05% Tween 20. Primary antibodies were diluted in the blocking solution and incubated overnight at 4°C. After 3 washes with PBS/0.05% Tween 20, membranes were incubated with horseradish peroxidase-coupled secondary for 1 hr at room temperature. Membranes were then washed 3 more times in PBS/0.01%Tween 20 and blots were developed with enhanced chemiluminescent western blotting substrate (Pierce).

Immunofluorescence staining and imaging

Fixed cells were washed 3 times for 5 min in PBS and incubated with the primary-antibody in GDB buffer (0.2% BSA, 0.8 M NaCl, 0.5% Triton X-100, 30 mM phosphate buffer, pH 7.4) overnight at 4°C. After 3 times washing with PBS, cells were incubated with secondary-antibodies in GDB buffer for 1 hr at room temperature. After washing, coverslips were mounted in Vectashield.

Brain sections were obtained from embryos at E17.5. Whole heads were fixed in 4% paraformaldehyde and submerged in 30% sucrose. Brains were placed in Jung Tissue freezing medium (Leica) and cut in 12 μm coronal sections. Sections were blocked with 10% normal goat serum in 0.2% Triton X-100 PBS for 1 hr and incubated with primary antibodies diluted in blocking buffer overnight at 4°C. After washing, sections were incubated with secondary antibody diluted in blocking buffer for 90 min and mounted using Vectashield mounting medium.

The following microscopy techniques were used: wide-field fluorescence microscopy and confocal laser-scanning microscopy for immunohisto- and immunocytochemistry. Neurons were imaged with the Nikon Eclipse 80i with Plan Apo VC 100x numerical aperture (NA) 1.40 oil, Plan Apo VC 60x NA 1.40 oil, Plan Fluor 40x NA 1.30 oil, and a Plan Fluor 10x NA 0.30 objective (Nikon), equipped with a CoolSNAP HQ2 CCD camera (Photometrics), or using a LSM700 confocal laser-scanning microscope (Zeiss) with a Plan-Apochromat 63x NA 1.40 oil DIC, EC Plan-Neofluar 40x NA1.30 Oil DIC and a Plan-Apochromat 20x NA 0.8 objective. Each confocal image was a z series of 5–10 images, each averaged 2 times, covering the entire region of interested from top to bottom. Maximum projections were done from the resulting z stack. For fluorescence intensity comparison, settings were kept the same for all conditions.

Live-cell imaging

Live-cell imaging experiments were performed in an inverted microscope Nikon Eclipse Ti-E (Nikon), equipped with a Plan Apo VC 100x NA 1.40 oil and a Plan Apo VC 60x NA 1.40 oil objective (Nikon), a Yokogawa CSU-X1-A1 spinning disk confocal unit (Roper Scientific), a Photometrics Evolve 512 EMCCD camera (Roper Scientific) and an incubation chamber (Tokai Hit) mounted on a motorized XYZ stage (Applied Scientific Instrumentation) which were all controlled using MetaMorph (Molecular

Devices) software. Two-color laser total-internal-reflection fluorescence (TIRF) microscopy with a 100x objective (Apo TIRF, NA1/4 1.49; Nikon), a Photometrics Evolve Delta 512 EMCCD camera (Roper Scientific) and an incubation chamber (Tokai Hit) was performed for KIF5B-GFP imaging experiments. Coverslips were mounted in metal rings and imaged using an incubation chamber that maintains temperature and CO_2 optimal for the cells (37°C and 5% CO_2). Neuron live imaging was performed in full conditioned medium and fresh medium was added to COS-7 before imaging.

Time-lapse live-cell imaging of GFP-MACF43 and mito-dsRed was performed with time acquisition intervals of 1sec for 2-3min. For MAP6-GFP imaged together with NPY-GFP/-RFP or RFP-Rab6, the time acquisition intervals were 100 ms for 20 s to 3 min. Imaging GFP-tagged MAP6 N-terminal fragment a time interval acquisition of 200 ms for 40 s was used. For KIF5B-GFP experiments, the time interval was 100 ms for 10-20 s. For MAP6-GFP imaging, the time acquisition interval was 1min for 3h, in COS-7 cells, and 10 min for overnight imaging in neurons.

Teem Photonics 355 nm Q-switched pulsed laser was used to perform laser-induced severing and study microtubule orientation in axons as describe previously (Yau et al., 2016). No signs of toxicity or blebbing of cells was observed during laser-induced severing.

Fluorescence recovery after photobleaching

The experiments were performed using the ILas2 system (Roper Scientific). A region at the proximal axon was bleached with high laser power and fluorescence recovery was observed for a period of 10min. For FRAP analysis, the mean intensity of the bleached area was corrected with background values, as well as the bleaching that occurred during image acquisition. Data were normalized with control fluorescence averaged over 5 initial frames before bleaching and stated as 100% intensity. Average curves were obtained and represented.

Drug treatments

For taxol-induced axon formation experiments, a concentration of 10nM for 48h was used. COS-7 cells were treated with 2-BP at concentrations of 50 μM (for immunocytochemistry) or 100 μM (in live-cell experiments), or PalB at 10 μM for 3h. In neurons, 2-BP and PalB treatments were done at concentrations of 10 μM for 3-4h. Ionomycin and BAPTA treatments were done using concetrations of 1 μM and 3.3 μM, respectively, for 6-7 hr.

Acyl Rac Assay

Acyl Rac Assays were performed as described previously with minor modifications (Forrester et al., 2011). Briefly, treated/transfected neurons (DIV2) were washed in PBS and collected in lysis buffer (25 mM HEPES, 25 mM NaCl, 1 mM EDTA, pH 7.5) containing protease inhibitor cocktail (Roche). Lysates were centrifuged at 20,000 g for 30 min. Amounts of protein of around 0.3 mg per reaction were used. Methyl methanethiosulfonate (MMTS) and SDS were added to supernants to final concentrations of 0.1% and 2.5%, respectively. The mixture was incubated at 40°C for 10 min with frequent vortexing. Proteins were precipitated by adding three volumes of cold acetone and incubating at −20°C for 20 min. After centrifugation at 5,000 g for 10 min, the pellet was washed with acetone and resuspended in 300 μL of binding buffer (100 mM HEPES, 1.0 mM EDTA, 1% SDS, pH 7.5) and added to 30 μL of prewashed thiopropyl Sepharose. To this mixture was added 40 μL of either freshly prepared 2 M NH 2 OH or 2 M NaCl. Binding reactions were incubated on a rotator at room temperature for 3 hr. Approximately 20 μL of each supernatant was saved as the ''total input.'' Resins were washed at least five times with binding buffer. For immunoblot analysis, elution was performed using 30 μL of SDS-page sample buffer containing DTT and boiled for 10 min.

Inducible cargo trafficking assay

The inducible cargo trafficking assay was performed as describe previously (Kapitein et al., 2010). Briefly, dissociated hippocampal neurons were co-transfected with GFP, FKBP-mRFP-PEX and KIF5B (1-807)-HA-FRB and pSuper control or MAP6 shRNA at DIV1 and imaged at DIV4. To induce specific binding of FRB and FKBP constructs, rapalog was added to a final concentration of 100nM. Within a maximum period of 40 min, different neurons were imaged for 3 min with an interval of 0.5 s.

Image analysis and quantification

Data were collected and analyzed from 2-5 independent experiments. No specific strategy for randomization and/or stratification was employed. The studies were blind in data analysis. Grubbs' test was performed to detect significant outliers.

Quantification of immunofluorescence intensity in neurons

Regions of interest of approximately 20 μm long were manually drawn in axons or dendrites using ImageJ. Mean intensity was measured from these regions, background values were subtracted and values were corrected to α-tubulin or β-III tubulin levels. These data were normalized to intensities in controls.

Polarity index

Regions of approximately 20 μm long were drawn from the soma into axons and at least 2 dendrites. Mean intensities in these regions were calculated using ImageJ. Background values were subtracted and values were corrected to α-tubulin or β-III tubulin levels. Polarity index (PI) was calculated using the following formula: PI = (Id-Ia)/(Id+Ia), where Id is the mean dendrite intensity and Ia is the mean axonal intensity. Non-polarized proteins present a PI = 0 (Id = Ia), whereas PI > 0 or PI < 0 indicates polarization toward dendrites or axons, respectively.

Analysis of knockdowns

Hippocampal neurons were transfected with either pSuper control or a shRNA against a specific MAP, together with a fill (BFP). Neurons were fixed 72 hr after transfection and co-stained with an antibody against the knocked down protein together with α-tubulin or β-III tubulin antibody. Mean intensities for the MAPs were quantified in dendrites or axons of control and depleted neurons using ImageJ software. Background values were subtracted and values were corrected to α-tubulin or β-III tubulin levels.

Analysis of MAP6 distribution in neurons

Plot profiles of MAP6, MAP2, Tau and Na_v channels were created from segmented lines traced from the soma along the axon in neurons using ImageJ.

Quantification of EB1-comet and NPY-positive vesicles number

ImageJ plugin ComDet (https://github.com/ekatrukha/ComDet) was used to quantify the number of EB1 comets or NPY-positive vesicles in soma, dendrites or distal axons. Numbers were normalized to the corresponding area or neurite length.

Analysis of neuronal morphology

For the analysis of axon morphology, BFP was used as a fill and axon was identified as the longest neurite. Quantifications were performed using ImageJ software and the NeuronJ plugin (Meijering et al., 2004). Total axonal length was calculated as the sum of the lengths of the axon and its branches.

Quantification of MAP6-positive vesicles and microtubules

100 μm^2 areas were randomly selected from control and treated COS-7 cells. Number of MAP6-positive vesicles and microtubules were quantified and averaged.

Quantification of vesicle colocalization

Number of vesicles labeled with only green, only red or labeled with both green and red markers was quantified. The percentage of green and red double-positive vesicles compared to the total number of green and red vesicles was calculated.

Pearson's coefficient quantification

Pearson's coefficient was determined using the JACoP plugin (Bolte and Cordelières, 2006) for ImageJ. For each cell, three ROIs were selected and Pearson's coefficient was average per cell.

Quantification of moving particles

Run length, time, and velocity of dynamic microtubules (labeled with GFP-MACF43), mitochondria (labeled with mito-ds Red), peroxisome (tracked with PEX3-RFP-FKBP) or KIF5B molecules (labeled with KIF5B(1-807)-GFP) were quantified from kymographs of proximal axons created using the Kymoreslicewide plug-in under Fiji.

To quantify the percentage of NPY-positive vesicles and vesicles containing N-terminal domain of MAP6 both moving and static vesicles from the approximately last 20 μm of axons were considered.

Quantification of western blot data

Densitometry of western blots was done using the gel analysis method of ImageJ software. Protein levels were normalized to loading controls.

QUANTIFICATION AND STATISTICAL ANALYSIS

All statistical details of experiments, including the definitions and exact values of n, and statistical tests performed, can be found in Figures and Figure Legends. n represents number of analyzed cells in all figures except for Figure 3A (n represents number of mitochondria), Figure 3I (n represents number of slices) and Figures 5A, 5B, and 8F (n represents number of experimental replications). Data processing and statistical analysis were done in Excel and GraphPad Prism (GraphPad Software). Significance was defined as: ns-not significant, $*p < 0.05$ $**p < 0.01$ and $***p < 0.001$. Statistical analysis include: Unpaired t test, Mann-Whitney U test, one-way ANOVA followed by a Tukey's multiple comparison test, Kruskal–Wallis test followed by a Dunn's Multiple Comparison Test, Two-ways ANOVA followed by Bonferroni post-test, Wilcoxon signed-rank test and Fisher's exact test with Bonferroni correction. The assumption of normality was checked using D'Agostino-Pearson omnibus test.